Low mass gluino within the sparticle landscape, implications for dark matter, and early discovery prospects at LHC-7

Ning Chen,[1] Daniel Feldman,[2] Zuowei Liu,[1] Pran Nath,[3] and Gregory Peim[3]

[1]*C. N. Yang Institute for Theoretical Physics, Stony Brook University, Stony Brook, New York 11794, USA*
[2]*Michigan Center for Theoretical Physics, University of Michigan, Ann Arbor, Michigan 48109, USA*
[3]*Department of Physics, Northeastern University, Boston, Massachusetts 02115, USA*

(Received 7 November 2010; published 4 February 2011)

We analyze supergravity models that predict a low mass gluino within the landscape of sparticle mass hierarchies. The analysis includes a broad class of models that arise in minimal and in nonminimal supergravity unified frameworks and in extended models with additional $U(1)_X^n$ hidden sector gauge symmetries. Gluino masses in the range (350–700) GeV are investigated. Masses in this range are promising for early discovery at the LHC at $\sqrt{s} = 7$ TeV (LHC-7). The models exhibit a wide dispersion in the gaugino-Higgsino eigencontent of their lightest supersymmetric particles and in their associated sparticle mass spectra. A signature analysis is carried out and the prominent discovery channels for the models are identified with most models needing only ~ 1 fb^{-1} for discovery at LHC-7. In addition, significant variations in the discovery capability of the low mass gluino models are observed for models in which the gluino masses are of comparable size due to the mass splittings in different models and the relative position of the light gluino within the various sparticle mass hierarchies. The models are consistent with the current stringent bounds from the Fermi-LAT, CDMS-II, XENON100, and EDELWEISS-2 experiments. A subclass of these models, which include a mixed–w-ino lightest supersymmetric particle and a Higgsino lightest supersymmetric particle, are also shown to accommodate the positron excess seen in the PAMELA satellite experiment.

DOI: 10.1103/PhysRevD.83.035005 PACS numbers: 12.60.Jv, 14.80.Ly, 95.35.+d

I. INTRODUCTION

The exploration of supersymmetry at colliders within the landscape of sparticle mass hierarchies can provide insight into the nature of the underlying theory [1–8]. Thus, in the minimal supersymmetric standard model there are 32 supersymmetric particles including the Higgs bosons and in general there exists a mass hierarchy among them. One can estimate the number of sparticle mass patterns that may appear by use of Stirling's formula [$n! \sim \sqrt{2\pi n}(n/e)^n$], which gives close to 10^{28} different possibilities including sum rules for the sparticle masses. Limiting oneself to the first four lightest sparticles and assuming that the lightest supersymmetric particle (LSP) is the neutralino, the number is significantly reduced but is still around $\mathcal{O}(10^4)$. On the other hand, in supergravity unified models with radiative breaking of electroweak symmetry, the number of allowed possibilities is much smaller [1–3]. Further, it has been demonstrated in several subsequent works [2–8] that analyses of supersymmetry from the point of view of the possible low mass sparticle hierarchies indeed shed light on the underlying theory as the specific mass orderings and mass gaps among sparticles dictate the type of signatures that would be produced at the Large Hadron Collider. Specifically, in this work we investigate the landscape under the constraint that the gluino has a low mass and is discoverable in early runs at the LHC at $\sqrt{s} = 7$ TeV and with a few fb^{-1} of integrated luminosity (for a recent review see [9]).

Because of their strong color interactions, gluinos and squarks are expected to be produced copiously in high energy pp collisions at the LHC, and a wide class of supergravity models are capable of such sparticle production. Several works have already appeared which point to encouraging results for the possibility of discovery of supersymmetry in the early data [10–17]. Here, our analysis of sparticle mass hierarchies is done within the context of supergravity grand unified models [18] where we include both universal and nonuniversal soft breaking [1–3,18–20] that allow for the possibility of low mass gluinos in the mass range of approximately (350–700) GeV, with sfermions that could be either light or heavy, consistent with all current experimental constraints. In addition, we study extended supergravity models where the relic density is satisfied by coannihilations with matter in the hidden sector [21,22] which is another possible particle physics solution, beyond a Breit-Wigner enhancement [23,24] and other mechanisms, to achieving a large flux of dark matter in the halo consistent with the relic density. Dark matter annihilations in a universe with a nonthermal cosmological history is a possible solution as well [25,26].

The class of models we consider within the context of sparticle mass hierarchies are those which are promising for early supersymmetry (SUSY) discovery. A number of models with low mass gluinos and their hierarchical mass patterns are exhibited, and their LHC signatures at $\sqrt{s} = 7$ TeV are analyzed and discussed. The strong

 © 2011 American Physical Society

correlations between the hierarchical structure of the sparticle masses [1] and the early discovery prospects at LHC as well as in dark matter experiments are studied with specific focus on the gluino in the mass hierarchy. It is shown that most of the models would become visible with (1–5) fb^{-1} of integrated luminosity. Further, the models are subjected to the more recent constraints from the Fermi Large Area Telescope (Fermi-LAT) data [27] on the monochromatic radiation that can arise in annihilation of neutralinos into photons, as well as from the direct detection experiments on the LSP-nucleon spin-independent cross sections [28–30] (for a recent overview see [31]) which are beginning to put more stringent constraints on supersymmetric models. It is also shown that a subclass of the models with a low mass gluino have a neutralino LSP that can satisfy the positron excess as seen in the PAMELA satellite experiment [32]. The low mass gluino (LG) models discussed are consistent with the cold dark matter relic density from the WMAP data [33], and most lie within the observed WMAP experimental band. The sparticle mass hierarchies corresponding to these LG models are given in Table II.

The outline of the rest of the paper is as follows: In Sec. II we discuss the experimental constraints on the model classes studied. These constraints include the recent limits from Fermi-LAT on the monochromatic radiation and the upper limit on the spin-independent LSP-nucleon elastic scattering cross section. In Sec. III we analyze a number of representative model points that encompass a wide range of theoretical frameworks which include minimal supergravity grand unification (mSUGRA), nonuniversal supergravity grand unified models (SUGRA), and extended supergravity models with a $U(1)_X^n$ hidden sector gauge symmetry. The specific properties of these models, including their light sparticle spectra, are also discussed in this section. A subclass of the models is shown to be capable of accommodating the PAMELA data. In Sec. IV we discuss the signatures of the models considered here at the LHC with $\sqrt{s} = 7$ TeV. Conclusions are given in Sec. V.

II. EXPERIMENTAL CONSTRAINTS

Below, we summarize current constraints on supersymmetric models from collider and dark matter experiments which we include in the analysis.

1. Collider constraints.—The models we consider are subject to several accelerator constraints which are sensitive to new physics. These include the experimental result $\mathcal{B}r(B \to X_s\gamma) = (352 \pm 23 \pm 9) \times 10^{-6}$ from the Heavy Flavor Averaging Group [34] along with *BABAR*, Belle, and CLEO, while for the standard model prediction we use the next-to-next-to-leading-order estimate of $\mathcal{B}r(b \to s\gamma) = (3.15 \pm 0.23) \times 10^{-4}$ [35]. Supersymmetry makes important corrections to this process [36], and the current (small) discrepancy between the experiment and the standard model predictions hints at the presence of low-lying sparticles [37]. For this analysis we take a 3σ corridor around the experimental value: $2.77 \times 10^{-4} < \mathcal{B}r(b \to s\gamma) < 4.27 \times 10^{-4}$. Another important flavor constraint is the rare decay process $B_s \to \mu^+\mu^-$. We take the recent 95% C.L. constraint by CDF [38]: $\mathcal{B}r(B_s \to \mu^+\mu^-) < 5.8 \times 10^{-8}$. In the context of a large spin-independent cross section in the minimal supersymmetric standard model (MSSM), which can occur at low Higgs masses, and large tanβ, this constraint has recently been shown to be very restrictive on the MSSM parameter space under radiative breaking [2], including models with low mass dark matter [39] in the 10 GeV range [40,41]. The correction to $g_\mu - 2$ is an important indication of new physics, and in models of supersymmetry, significant corrections are expected with a low-lying sparticle spectrum [42]. The $g_\mu - 2$ data [43] have been analyzed recently using improved estimates of the hadronic correction [44]. In this analysis we take a conservative bound: $-11.4 \times 10^{-10} < \delta(g_\mu - 2) < 9.4 \times 10^{-9}$. Experimental limits on the sparticle masses are as discussed in [37].

2. Dark matter constraints.—In addition to the above, there are constraints from dark matter experiments. The seven-year WMAP data [33] give the relic density of cold dark matter as $\Omega_{\rm DM}h^2 = 0.1109 \pm 0.0056$. For our analysis, we take a conservative upper bound on the relic density predictions in the MSSM to take into account the theoretical uncertainties and other possible dark matter contributions (see, e.g., [24,45,46]; for early work see [47]).

TABLE I. A sample of low mass gluino models where additionally we take $\mu > 0$ and $m_{t(\rm pole)} = 173.1$ GeV. The soft breaking parameters are given at the high scale of $\sim 2 \times 10^{16}$ GeV. Nonuniversalities in the gaugino sector $M_{a=1,2,3}$ are taken in 15 of the models. All masses in the table are in GeV. A more detailed discussion of the models is given in the text.

Label	$M_{\tilde{g}}$	m_0	M_1	M_2	M_3	A_0	tanβ
LG1	424	2000	130	130	130	−1000	8
LG2	715	60	300	300	300	−100	8
LG3	386	1400	800	528	132	3000	25
LG4	378	3785	836	508	98	−6713	20
LG5	385	2223	859	843	130	4680	48
LG6	391	1180	860	790	138	2692	42
LG7	442	2919	263	151	138	4206	18
LG8	417	1303	257	152	139	1433	18
LG9	696	1845	327	193	249	1898	13
LG10	365	1500	1600	1080	120	2100	15
LG11	433	605	302	176	161	1781	22
LG12	588	636	419	249	228	1568	37
LG13	684	335	391	466	279	−1036	3
LG14	618	48	289	310	256	−407	6
LG15	602	61	310	351	249	0	9
LG16	343	2200	450	235	100	300	5
LG17	425	3000	400	207	125	0	4

However many of the models produce a relic abundance consistent with the double-sided WMAP bound at a few standard deviations. Further, new experimental results from probes of direct and indirect detection of dark matter have begun to place more stringent bounds on dark matter models. Thus, recent results from direct detection experiments CDMS-II [28], XENON100 [29], and EDELWEISS-2 [30] suggest an upper bound to the spin-independent (SI) LSP-nucleon scattering cross section. At present, the limit is $\sigma_{\rm SI} \lesssim 5 \times 10^{-8}$ pb over the range of interest of the models discussed here. Many of the models discussed here have spin-independent cross sections in the range $\lesssim (10^{-9}$–$10^{-8})$ pb and are thus directly relevant for dark matter direct detection experiments in the future.

Further, the Fermi-LAT experiment has obtained constraints on the production of γ-ray lines with energies from 30 to 200 GeV. The upper limits of the γ-ray line flux are in the range of $(0.6$–$4.5) \times 10^{-9}$ cm^{-2} s^{-1} [27]. This gives rise to upper bounds on the corresponding dark matter annihilation cross sections, and as we will discuss later, the data constrain the eigencontent of the LSP in the mass range analyzed. Finally, the recent PAMELA [32] data show an anomalous high positron flux in the range (10–100) GeV. The possible dominant contribution to the positron excess in the MSSM with neutralino dark matter can arise from $\tilde{\chi}_1^0 \tilde{\chi}_1^0 \to W^+W^-, ZZ$ annihilations, depending on the eigencontent of the LSP. Here, a velocity averaged cross section on the order of $\langle \sigma v \rangle_{WW+ZZ} \gtrsim 5 \times 10^{-25}$ cm^3 s^{-1} will be shown to provide a reasonable explanation of the data without invoking large astrophysical boost factors in the positron flux. We will consider the implications of such constraints later in the analysis.

III. MODELS OF A LOW MASS GLUINO AND SPARTICLE MASS HIERARCHIES

In $N = 1$ supergravity unified models, gaugino masses can arise from the gauge kinetic function f_a corresponding to the gauge group G_a. Thus, for the standard model gauge groups $SU(3)_C$, $SU(2)_L$, and $U(1)$ the gaugino masses are given by $M_a = (2\mathcal{R}(f_a))^{-1} F^I \partial_I f_a$ $(a = 1, 2, 3)$, where the gauge kinetic function f_a depends on the fields ϕ_I and F^I are the order parameters for supersymmetry breaking with the vacuum expectation value of F^I proportional to the gravitino mass, i.e., $\propto m_{3/2} M_P$. The assumption that the fields ϕ_I are singlets of the standard model gauge group will lead to universal gaugino masses. However, in general the breaking can occur involving both singlet and non-singlet terms (for a recent analysis see [48]) and, thus, the gaugino masses in general will not be universal. Additionally, there can be loop corrections to the gaugino masses via exchange of heavy fields where the leading corrections are also proportional to $m_{3/2}$, to the Casimir, and to the square of the gauge coupling for each gauge group (for early work see [49]).

A case of immediate interest for LHC analyses is $M_3(M_U) \in (100$–$300)$ GeV as the gluino mass at the

TABLE II. Sparticle mass hierarchies for the low mass gluino models. Listed are the first six lightest sparticles in the spectra. The lightest squark, shown in column 4, is taken from the first 2 generations. In the display of the mass hierarchies we do not include the light CP even Higgs.

Label	Mass pattern	$M_{\tilde{g}}$ (GeV)	Lightest $M_{\tilde{q}}$ (GeV)	Gluino position
LG1	$\tilde{\chi}_1^0 < \tilde{\chi}_1^\pm < \tilde{\chi}_2^0 < \tilde{g} < \tilde{\chi}_3^0 < \tilde{\chi}_4^0$	424	1985	4
LG2	$\tilde{\chi}_1^0 < \tilde{\tau}_1 < \tilde{\ell}_R < \tilde{\nu}_\tau < \tilde{\nu}_\ell < \tilde{\ell}_L$	715	635	31
LG3	$\tilde{\chi}_1^0 < \tilde{g} < \tilde{\chi}_1^\pm < \tilde{\chi}_2^0 < \tilde{t}_1 < \tilde{\chi}_3^0$	386	1411	2
LG4	$\tilde{\chi}_1^0 < \tilde{g} < \tilde{\chi}_1^\pm < \tilde{\chi}_2^0 < \tilde{t}_1 < \tilde{\chi}_3^0$	378	3751	2
LG5	$\tilde{\chi}_1^0 < \tilde{g} < \tilde{\chi}_1^\pm < \tilde{\chi}_2^0 < \tilde{t}_1 < \tilde{\tau}_1$	385	2217	2
LG6	$\tilde{\chi}_1^0 < \tilde{t}_1 < \tilde{g} < \tilde{\chi}_1^\pm < \tilde{\chi}_2^0 < \tilde{\chi}_3^0$	391	1202	3
LG7	$\tilde{\chi}_1^0 < \tilde{\chi}_1^\pm < \tilde{\chi}_2^0 < \tilde{g} < \tilde{\chi}_3^0 < \tilde{\chi}_4^0$	442	2888	4
LG8	$\tilde{\chi}_1^0 < \tilde{\chi}_1^\pm < \tilde{\chi}_2^0 < \tilde{g} < \tilde{\chi}_3^0 < \tilde{\chi}_4^0$	417	1314	4
LG9	$\tilde{\chi}_1^0 < \tilde{\chi}_1^\pm < \tilde{\chi}_2^0 < \tilde{\chi}_3^0 < \tilde{\chi}_4^0 < \tilde{\chi}_2^\pm$	696	1882	7
LG10	$\tilde{\chi}_1^0 < \tilde{\chi}_1^\pm < \tilde{\chi}_2^0 < \tilde{g} < \tilde{\chi}_3^0 < \tilde{t}_1$	365	1511	4
LG11	$\tilde{\chi}_1^0 < \tilde{\chi}_1^\pm \lesssim \tilde{\chi}_2^0 < \tilde{t}_1 < \tilde{g} < \tilde{b}_1$	433	690	5
LG12	$\tilde{\chi}_1^0 < \tilde{\chi}_1^\pm < \tilde{\chi}_2^0 < \tilde{\tau}_1 < \tilde{\chi}_3^0 < \tilde{\chi}_4^0$	588	790	14
LG13	$\tilde{\chi}_1^0 < \tilde{t}_1 < \tilde{\chi}_1^\pm < \tilde{\chi}_2^0 < \tilde{\tau}_1 < \tilde{\ell}_R$	684	677	24
LG14	$\tilde{\chi}_1^0 < \tilde{\tau}_1 < \tilde{\ell}_R < \tilde{\nu}_\tau < \tilde{\nu}_\ell < \tilde{\ell}_L$	618	550	31
LG15	$\tilde{\chi}_1^0 < \tilde{\tau}_1 < \tilde{\ell}_R < \tilde{\nu}_\tau < \tilde{\nu}_\ell < \tilde{\chi}_1^\pm$	602	536	31
LG16	$\tilde{\chi}_1^0 < \tilde{\chi}_1^\pm < \tilde{\chi}_2^0 < \tilde{g} < \tilde{\chi}_3^0 < \tilde{\chi}_2^\pm$	343	2178	4
LG17	$\tilde{\chi}_1^0 < \tilde{\chi}_1^\pm < \tilde{\chi}_2^0 < \tilde{g} < \tilde{\chi}_3^0 < \tilde{\chi}_2^\pm$	425	2966	4

unified scale (M_U) increases in magnitude as one moves towards the electroweak scale via the renormalization group equations, and this translates to gluino masses in the range of (350–750) GeV in the model classes considered. While the models considered in this analysis can be obtained with specific choices of supersymmetry breaking, involving, for example, a combination of singlet and nonsinglet F-term breaking for gaugino masses at the scale M_U, we will keep our analysis rather generic in that the information on symmetry breaking is contained in the gaugino masses at the grand unified theory (GUT) scale which can arise from various models of the gauge kinetic energy function, and in general they depend on both the hidden and the visible GUT sector fields.

Indeed there are several classes of well motivated SUGRA models which lead to sparticle spectra with a low mass gluino. These include the mSUGRA models and nonuniversal SUGRA models where the soft breaking in the gaugino sector at the grand unification scale includes nonsinglet contributions as well as singlet and nonsinglet contributions (see, e.g., [48,50]). Different high scale models can generate different next-to-lightest supersymmetric particles (NLSPs) at the electroweak scale, some of which lead to the gluino as the NLSP (GNLSP models) uncovered in Ref. [2] and further investigated in [50–52]. We also discuss models where the relic density due to thermal annihilations is rather small but can be boosted to the current range of the WMAP value with coannihilations with matter in the hidden sector [22]. Such a situation arises in SUGRA models with extended $U(1)_X^n$ gauge groups [22]. Another possibility to boost the relic density arises from nonthermal processes [25]. Both of these model classes, with different types of cosmological histories, namely, thermal [17,22] and nonthermal [25,26], can lead to an explanation of the positron excess seen by the PAMELA satellite experiment and provide explanations for the relic abundance of dark matter—however, both classes require fields beyond those in the low energy MSSM.

We give a broad sample of models in Table I, where the SUGRA model parameters at the GUT scale are exhibited. The parameters include the universal scalar mass m_0, the three gaugino masses $M_{1,2,3}$, the universal trilinear coupling A_0, and the ratio of the two Higgs vacuum expectation values, $\tan\beta$. These models satisfy the stringent Fermi-LAT constraints on $\gamma\gamma$ and γZ cross sections as discussed later. The sparticle mass hierarchies corresponding to these models are given in Table II. In Fig. 1 we give a display of the significance for several optimal channels for a sample of the model classes at 1 fb^{-1} of integrated luminosity at $\sqrt{s} = 7$ TeV. One finds that all of the models shown are visible in several channel except for LG3 and LG4, which are visible only in a small number of channels. We discuss these results in depth in Sec. IV. A more detailed discussion of these model classes follows.

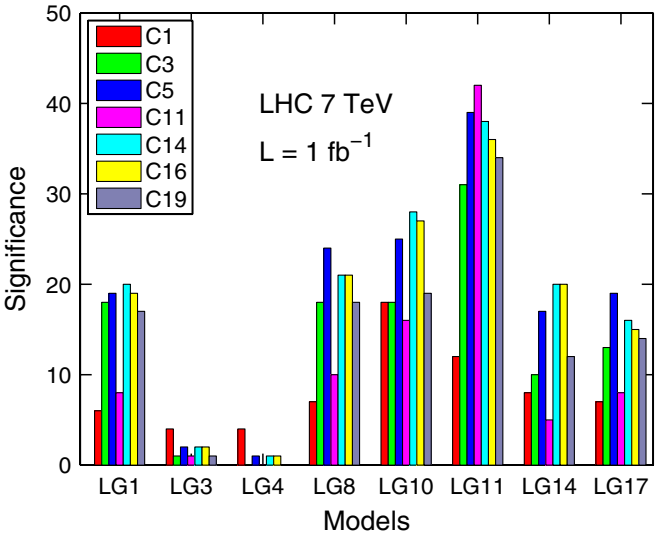

FIG. 1 (color online). A summary of the significance (SUSY signal divided by the square root of the SM background) for various signature channels and cuts (C) for a subset of the LG mass models with an integrated luminosity of 1 fb^{-1} at the LHC for $\sqrt{s} = 7$ TeV. We will discuss in detail in Sec. IV how these drastic variations come about even though the gluino masses here are confined to the range ~(350–700) GeV for all models.

1. Low mass gluinos in mSUGRA.—The possibility that a low mass gluino and heavy scalars can arise in the radiative breaking of the electroweak symmetry in SUGRA models was seen early on [53]. It was later realized that this phenomenon is more general, and the hyperbolic branch (HB) or the focus point region of radiative breaking of the electroweak symmetry was discovered where scalars are heavy and gauginos are light [34]. In the analysis of [2], it was found that on the HB the chargino is predominantly the NLSP over a very broad class of soft breaking models.[1]

However, a low mass gluino, around 400 GeV, can arise in minimal supergravity if the neutralinos annihilate near the Z pole or near the Higgs poles [56]. Specifically a low mass gluino arises in mSUGRA in the sparticle mass landscape which was labeled as mSP4 in [1] where the first four sparticles have the mass hierarchy as follows:

$$\text{LG1: } \tilde{\chi}_1^0 < \tilde{\chi}_1^\pm < \tilde{\chi}_2^0 < \tilde{g}, \qquad M_{\tilde{g}} = 424 \text{ GeV}. \quad (1)$$

An illustration of such a model is given by LG1 in Table III. In this case the LSP is essentially dominated by the b-ino component[2] as can be seen from Table III. The model LG1 has a low mass gluino of about 420 GeV, and the relic density is within the WMAP band due to neutralino annihilations near the Higgs pole. It is easily

[1]HB models with larger Higgsino components and with a light gluino have been studied in [1–3,34,50,54,55], and Ref. [1] of [24].

[2]We use the notation Z_{11}, Z_{12}, Z_{13}, Z_{14} for the eigencomponents of the lightest neutralino, namely, the b-ino, the w-ino, and the two Higgsinos.

TABLE III. mSUGRA models of a low mass gluino and a display of some of the lighter masses within the sparticle mass hierarchies. In model LG1 the neutralino, the chargino, and the gluino are all light while the SUSY scalars are heavy. This model generates the relic density in the WMAP band via the annihilation of the neutralinos near the Higgs pole. However, in model LG2 the scalars are also light and the relic density lies in the WMAP band via coannihilations of the neutralinos with the stau and other light sleptons. All masses are in GeV.

Label	M_h	$M_{\tilde{\chi}_1^0}$	$M_{\tilde{\chi}_1^\pm}$	$M_{\tilde{g}}$	$M_{\tilde{\tau}_1}$	$M_{\tilde{t}_1}$	M_A	$M_{\tilde{b}_1}$	Z_{11}	Z_{12}	Z_{13}	Z_{14}	$\sigma^{\rm SI}_{\tilde{\chi}_1^0 p}$ (cm^2)
LG1	115	53	104	424	1983	1118	2040	1610	0.993	−0.051	0.103	−0.025	5.4×10^{-46}
LG2	111	118	220	715	126	476	463	606	0.990	−0.044	0.127	−0.051	5.2×10^{-45}

seen that the model LG1 is on the HB and, thus, has heavy scalars. Since the neutralino is b-ino-like, this leads to scaling of the gaugino mass spectra [57]. Further, because the neutralino has a suppressed Higgsino content, the spin-independent scattering is suppressed at the level of $\sim 5\times10^{-46}$ cm^2.

A diametrical situation holds for the model point LG2. While the gluino is still light in this model, lying in the sub-TeV region, it is actually the heaviest sparticle in the whole sparticle spectrum. Specifically the hierarchy is

$$\text{LG2: } \tilde{\chi}_1^0 < \tilde{\tau}_1 < \tilde{\ell}_R < \tilde{\nu}_\tau < \cdots < \tilde{g},$$
$$M_{\tilde{g}} = 715 \text{ GeV}. \tag{2}$$

The relic density in the model LG2 is satisfied via coannihilations [58] with the stau and with the other sleptons. Since model LG2 has a lighter scalar sparticle spectrum, it has a larger spin-independent cross section than LG1 by a factor of about 10. The ordering of the gluino mass in the hierarchy will have dramatic effects on the signals at the LHC which we will discuss in detail shortly.

2. Low mass gluinos in nonuniversal SUGRA models.—Low mass gluinos can arise from models where the gaugino masses are in general nonuniversal at the GUT scale, as for instance, from a combination of singlet and non-singlet F term breaking as discussed in the beginning of this section. Models LG3–LG17 in Table I fall in this class. Such models can lead to a low mass gluino that can be the NLSP, the next-to-next-to-lightest supersymmetric particle (NNLSP), etc. The case when the gluino is the NLSP requires special attention since here the relic density can be satisfied by the neutralino coannihilations with the gluino, as in the model LG3. This case was discussed at length in [50,52,59]. For the models discussed in Table IV, which have a GNLSP with a rather low mass gluino (i.e., below 400 GeV), the sparticle mass hierarchies are given by [50]

$$\text{(LG3, LG4, LG5): } \tilde{\chi}_1^0 < \tilde{g} < \tilde{\chi}_1^\pm < \tilde{\chi}_2^0 < \tilde{t}_1,$$
$$M_{\tilde{g}} = (386, 378, 385) \text{ GeV}. \tag{3}$$

Since the gluino coannihilation in the GNLSP model is a relatively new entry among the ways dark matter originates in the early Universe, we summarize the main features of the relic density calculation here first, before discussing the relevant features of this class of models that enter in the LHC signature analysis. Thus, for a GNLSP the relic density depends strongly on coannihilation effects which are controlled by the Boltzmann factor [58]

$$\gamma_i = \frac{n_i^{\rm eq}}{n^{\rm eq}} = \frac{g_i(1+\Delta_i)^{3/2}e^{-\Delta_i x}}{\sum_j g_j(1+\Delta_j)^{3/2}e^{-\Delta_j x}}, \tag{4}$$

where g_i are the degrees of freedom of χ_i, $x = m_1/T$, and $\Delta_i = (m_i - m_1)/m_1$, with m_1 defined as the LSP mass. Thus, for the analysis of the relic density, the effective annihilation cross section $\sigma_{\rm eff}$ can be written approximately as

$$\sigma_{\rm eff} = \sum_{i,j}\gamma_i\gamma_j\sigma_{ij} \simeq \sigma_{\tilde{g}\tilde{g}}\gamma_{\tilde{g}}^2 + 2\sigma_{\tilde{g}\tilde{\chi}_1^0}\gamma_{\tilde{g}}\gamma_{\tilde{\chi}_1^0} + \sigma_{\tilde{\chi}_1^0\tilde{\chi}_1^0}\gamma_{\tilde{\chi}_1^0}^2$$
$$\simeq \sigma_{\tilde{g}\tilde{g}}\gamma_{\tilde{g}}^2, \tag{5}$$

where we have used the fact that the gluino annihilation cross sections are usually much larger than the LSP annihilation even with inclusion of the Boltzmann factor and

$$\sigma(\tilde{g}\,\tilde{g} \to q\bar{q}) = \mathcal{E}_q\frac{\pi\alpha_s^2\bar{\beta}}{16\beta s}(3-\beta^2)(3-\bar{\beta}^2), \tag{6}$$

TABLE IV. A display of the lighter sparticle masses within the mass hierarchies, and other attributes of GNLSP models with low mass gluinos. The mass splitting between the gluino and neutralino is between ∼(1–50) GeV for these models. Further details are given in the text. All masses are in GeV.

Label	M_h	$M_{\tilde{\chi}_1^0}$	$M_{\tilde{\chi}_1^\pm}$	$M_{\tilde{g}}$	$M_{\tilde{\tau}_1}$	$M_{\tilde{t}_1}$	M_A	$M_{\tilde{b}_1}$	Z_{11}	Z_{12}	Z_{13}	Z_{14}	$\sigma^{\rm SI}_{\tilde{\chi}_1^0 p}$ (cm^2)
LG3	112	340	429	386	1253	455	1421	995	0.997	−0.026	0.067	−0.029	6.3×10^{-46}
LG4	125	377	454	378	3529	1244	3888	2615	0.999	−0.006	0.021	−0.005	8.4×10^{-48}
LG5	117	365	660	385	1081	679	1167	1321	0.999	−0.003	0.039	−0.012	2.1×10^{-46}

$$\sigma(\tilde{g}\,\tilde{g} \to gg) = \mathcal{E}_g \frac{3\pi\alpha_s^2}{16\beta^2 s}\left\{\log\frac{1+\beta}{1-\beta}[21 - 6\beta^2 - 3\beta^4] - 33\beta + 17\beta^3\right\}, \quad (7)$$

where the nonperturbative corrections to the annihilation cross section can arise via multiple gluon exchange, giving rise to a Sommerfeld enhancement factor $\mathcal{E}$. These effects may be approximated by [60]

$$\mathcal{E}_j = \frac{C_j\pi\alpha_s}{\beta}\left[1 - \exp\left\{-\frac{C_j\pi\alpha_s}{\beta}\right\}\right]^{-1}, \quad (8)$$

where $C_{j=g} = 1/2(C_{j=q} = 3/2)$ for $\tilde{g}\,\tilde{g} \to gg(\tilde{g}\,\tilde{g} \to q\bar{q})$. In the above $\beta = \sqrt{1 - 4m_{\tilde{g}}^2/s}$, and $\bar{\beta} = \sqrt{1 - 4m_q^2/s}$. Although the gluino annihilation cross section $\sigma_{\tilde{g}\,\tilde{g}}$ varies with gluino mass, the Boltzmann suppression factor $\gamma_{\tilde{g}}$ controls the contribution to the $\sigma_{\rm eff}$ so that the relic density of the b-ino-like neutralino is consistent with WMAP. We note that the effects of the Sommerfeld enhancement on the gluino cross sections can increase $\Delta_{\tilde{g}}$ by a small amount for a b-ino-like LSP $\sim$(2–3)% [50,59]. Such an increase in the mass gap between the gluino and the neutralino can potentially enhance the discovery reach of this class of models at the LHC as the mass gap between the $\tilde{g}$ and $\tilde{\chi}_1^0$ plays a crucial role in the strength of the LHC signals [50] which we will discuss in detail later. Three GNLSP models are exhibited in Table IV. Some of their pertinent spectra and other attributes, including their spin-independent cross sections, are also given in Table IV. It is seen from this table the neutralino is dominantly a b-ino. For each of these models gluino coannihilation dominates the relic density calculations. In the absence of additional hidden sector gauge groups (to be discussed in what follows), only LG3 lies in the WMAP band, while models LG4 and LG5 each have a reduced relic abundance and reduced mass gaps between $\tilde{g}$ and $\tilde{\chi}_1^0$.

Next we consider five models, LG6–LG10, in Table I where the gluino is light and in some cases it is the next-to-next-to LSP (GNNLSP). Specifically the sparticle mass hierarchies are

$$\begin{aligned}
&\text{LG6: } \tilde{\chi}_1^0 < \tilde{t}_1 < \tilde{g} < \tilde{\chi}_1^\pm < \tilde{\chi}_2^0, \quad M_{\tilde{g}} = 391 \text{ GeV};\\
&\text{LG7: } \tilde{\chi}_1^0 < \tilde{\chi}_1^\pm < \tilde{\chi}_2^0 < \tilde{g} < \tilde{\chi}_3^0, \quad M_{\tilde{g}} = 442 \text{ GeV};\\
&\text{LG8: } \tilde{\chi}_1^0 < \tilde{\chi}_1^\pm < \tilde{\chi}_2^0 < \tilde{g} < \tilde{\chi}_3^0, \quad M_{\tilde{g}} = 417 \text{ GeV};\\
&\text{LG9: } \tilde{\chi}_1^0 < \tilde{\chi}_1^\pm < \tilde{\chi}_{2,3,4}^0 < \tilde{\chi}_2^\pm < \tilde{g}, \quad M_{\tilde{g}} = 696 \text{ GeV};\\
&\text{LG10: } \tilde{\chi}_1^0 < \tilde{\chi}_1^\pm < \tilde{\chi}_2^0 < \tilde{g} < \tilde{\chi}_3^0 < \tilde{t}_1, \quad M_{\tilde{g}} = 365 \text{ GeV}.
\end{aligned} \quad (9)$$

Their relevant sparticle spectra and other attributes including eigencontent and spin-independent cross sections are displayed in Table V. Here the NLSP can be the stop or the chargino, while the LSP is a mixture of b-ino, w-ino, and Higgsino. The specific nature of the neutralino eigencontent makes these models significantly different from each other and from other light gluino models. This includes an interesting subclass of models where the LSP is dominantly Higgsino (LG10). Such a model class was recently analyzed [17] in the context of both the PAMELA positron excess and the Fermi-LAT photon line data.

Finally, in Table VI we give five models, LG11–LG15 where in addition to the low mass gluino one also has a light stau and a light stop (due to the smaller GUT value of m_0) along with a light chargino. Models LG11–LG15 have compressed sparticle spectra with the heaviest sparticle mass around 850 GeV. Model LG11 has a highly reduced overall mass scale of the sparticles, with a low mass gluino and a light stop with the mass hierarchy

$$\text{LG 11: } \tilde{\chi}_1^0 < \tilde{\chi}_1^\pm < \tilde{\chi}_2^0 < \tilde{t}_1 < \tilde{g}, \qquad M_{\tilde{g}} = 433 \text{ GeV}, \quad (10)$$

with the remaining sparticles in the mass range (500–700) GeV. In each of these models the relic density can be satisfied via coannihilations with different superparticles, and, in particular, model LG13 proceeds via stop coannihilations. For LG12, the gluino mass lies in the middle of the sparticle mass spectra, while for (LG13–LG15) the gluino mass is close to being the largest mass even though it is still relatively light, i.e., $M_{\tilde{g}} < 700$ GeV. Models LG11 and LG13 have rather low-lying light Higgs. However, the extraction of the Higgs mass from LEP data

TABLE V. The spectrum of low mass sparticles including the GNNLSP models within the sparticle mass hierarchies, and other attributes of models in nonuniversal supergravity grand unification with a low mass gluino. Model LG6 is a GNNLSP, and models LG7, LG8, and LG9 are effectively GNNLSP as the chargino and second-heaviest neutralino are roughly mass degenerate. LG10 has a mass splitting between the chargino and the neutralino of $\sim$5 GeV and is effectively a GNNLSP model. All masses are in GeV.

Label	M_h	$M_{\tilde{\chi}_1^0}$	$M_{\tilde{\chi}_1^\pm}$	$M_{\tilde{g}}$	$M_{\tilde{\tau}_1}$	$M_{\tilde{t}_1}$	M_A	$M_{\tilde{b}_1}$	Z_{11}	Z_{12}	Z_{13}	Z_{14}	$\sigma^{\rm SI}_{\tilde{\chi}_1^0 p}$ (cm^2)
LG6	109	359	570	391	737	378	839	833	0.992	−0.020	0.109	−0.064	6.6×10^{-45}
LG7	119	108	120	442	2786	1357	2947	2185	0.998	−0.049	0.039	−0.006	2.4×10^{-47}
LG8	112	104	117	417	1255	718	1284	1032	0.968	−0.202	0.143	−0.041	2.7×10^{-45}
LG9	115	135	152	696	1811	1067	1874	1513	0.985	−0.136	0.098	−0.030	7.8×10^{-46}
LG10	112	111	115	365	1570	734	1609	1323	0.058	−0.075	0.721	−0.686	7.3×10^{-45}

TABLE VI. An exhibition of the light sparticle masses within the hierarchies in models with low mass gluinos that are accompanied by light staus and light stops. The light Higgs masses for these models lie in the range (103–111) GeV and are generally lighter than the models where the chargino or the gluino is the NLSP shown in the previous tables, as the scalars in such a model are much heavier. All masses are in GeV.

Label	M_h	$M_{\tilde{\chi}_1^0}$	$M_{\tilde{\chi}_1^\pm}$	$M_{\tilde{g}}$	$M_{\tilde{\tau}_1}$	$M_{\tilde{t}_1}$	M_A	$M_{\tilde{b}_1}$	Z_{11}	Z_{12}	Z_{13}	Z_{14}	$\sigma^{\rm SI}_{\tilde{\chi}_1^0 p}$ (cm^2)
LG11	103	121	134	433	516	271	701	489	0.978	−0.171	0.117	−0.032	6.6×10^{-45}
LG12	107	169	190	588	424	489	551	602	0.973	−0.171	0.146	−0.058	3.0×10^{-44}
LG13	104	160	359	684	365	187	845	604	0.996	−0.023	0.076	−0.041	2.0×10^{-45}
LG14	111	114	227	618	118	338	478	514	0.990	−0.043	0.124	−0.052	4.7×10^{-45}
LG15	109	121	238	602	132	397	398	525	0.979	−0.052	0.177	−0.083	1.7×10^{-44}

is model-dependent, and we retain these models in the analysis pending further experimental data.

3. Low mass gluinos in extended SUGRA models and PAMELA data.—Recently, the PAMELA Collaboration [32] has included an analysis of statistical uncertainties in the positron fraction [61] and presented its results on the absolute $\bar{p}$ flux [62]. Models LG10, LG16, and LG17 in Table I have low mass gluinos with many other desirable features. Specifically, they can explain the positron excess in the PAMELA satellite experiment [32] (for previous experiments see [63]). However, their relic density by the usual thermal annihilation processes is rather small. This situation can be modified at least in two ways.

First, the relic density could be enhanced via coannihilation with matter in the hidden sector. For example, an extended Abelian gauge symmetry can arise from the hidden sector and can couple to the MSSM sector via mass mixing or kinetic mixing with the hypercharge field. The mass mixing arises via the Stueckelberg mechanism and the kinetic mixing via mixing of the hidden sector field strength and the hypercharge field strength. Such mixings can lead to an enhancement of the relic density which we now discuss. Thus, we consider for specificity the mass growth via the Stueckelberg mechanism allowing for mixings between the hypercharge gauge multiplet (Y_μ, λ_Y, $\bar{\lambda}_Y$, D_Y) and the gauge multiplet of $U(1)_X$ (X_μ, λ_X, $\bar{\lambda}_X$, D_X) both taken in the Wess-Zumino gauge. The effective Lagrangian contains the mixing terms [21,22,64]

$$-\tfrac{1}{2}(\partial_\mu\sigma + M_Y Y_\mu + M_X X_\mu)^2 + [\psi_{\rm st}(M_X\lambda_X + M_Y\lambda_Y) + \text{H.c.}], \quad (11)$$

where the axionic field σ arises from a chiral multiplet $S = (\rho + i\sigma, \psi_{\rm st}, F_S)$. The fields $\psi_{\rm st}$ and λ_X produce two Majorana spinors (hidden sector neutralinos) which mix with the neutralinos in the visible sector via the mass mixing given by Eq. (11). In addition the hidden sector neutralinos can mix with the visible sector via kinetic mixing [21,65]

$$-\frac{\delta}{2}X_{\mu\nu}Y^{\mu\nu} - i\delta(\lambda_X\sigma\cdot\partial\bar{\lambda}_Y + (Y\leftrightarrow X)) + \delta D_X D_Y. \quad (12)$$

We note that M_Y:M_X and δ are constrained to be small by fits to the precision electroweak data [66] and thus the additional neutralino states are weakly coupled to the MSSM.

An estimate of the bound on the (mass or kinetic) mixing can be obtained from studying eigenvalues of the vector sector. One finds the mixing is constrained for masses near the Z pole as derived in the first reference of [66]:

$$|\epsilon| \lesssim 0.05\sqrt{1 - m_1^2/m_2^2}, \quad (13)$$

where ϵ is the overall mass and/or kinetic mixing and $m_{(1,2)}$ is the mass of the hidden sector vector boson, or the Z boson mass, depending on which side of the Z pole the hidden sector mass resides. We add that dark matter with Stueckelberg mass growth and/or kinetic mixing, with a massive hidden $U(1)$ [21] has also appeared in Ref. [67] in various contexts.

The analysis above can be extended to a $U(1)_X^n$ gauge group in the hidden sector that produces $2n$ additional Majorana fields in the hidden sector, which we denote collectively by ξ_k^h ($k = 1-2n$). This extended set of hidden sector Majoranas will mix with the visible sector via mass mixing and kinetic mixing, where we again take the mixings to be small. Because of the small mixings between the visible and the hidden sector Majoranas, the LSP in the visible sector will have a small component which lies in the hidden sector, and as such, the eigencontent of the LSP is modified so that [21,22,64,68]

$$\tilde{\chi}_1^0 = Z_{11}\tilde{B} + Z_{12}\tilde{W} + Z_{13}\tilde{H}_1 + Z_{14}\tilde{H}_2 + \sum_{k=1}^{2n} Z_{1k}^h \xi_k^h, \quad (14)$$

where ξ_k^h are the hidden sector neutralinos (stinos) composed of the hidden sector gauginos and the hidden sector chiral fields as discussed above and Z_{1k}^h record the leakage into the hidden sector. Because of the small mixings between the visible and the hidden sector, the Z_{1k}^h are rather small, typically less than 1% of the components in the visible sector. For this reason we do not record them in Table VII and elsewhere. However, we will assume that the overall mixing is large enough so that the extra-weakly interacting states [21,69] remain in contact with the thermal bath. Specifically, we envision mixings in the range (10^{-5}–10^{-2}). In what follows, in the context of the PAMELA data, we will assume that the hidden sector

TABLE VII. An exhibition of the sparticle mass hierarchies in low mass gluino models which can explain the PAMELA positron excess. The models are consistent with data from the Fermi-LAT [27], CDMS-II [28], XENON100 [29], and EDELWEISS-2 [30] experiments. In the above we do not list the component of the neutralino lying in the hidden sector as it is typically small, i.e., $Z^h_{1k} < 1\%$.

Label	M_h	$M_{\tilde{\chi}^0_1}$	$M_{\tilde{\chi}^\pm_1}$	$M_{\tilde{g}}$	$M_{\tilde{\tau}_1}$	$M_{\tilde{t}_1}$	M_A	$M_{\tilde{b}_1}$	Z_{11}	Z_{12}	Z_{13}	Z_{14}	$\sigma^{\rm SI}_{\tilde{\chi}^0_1 p}$ (cm^2)
LG10	112	111	115	365	1570	734	1609	1323	0.058	−0.075	0.721	−0.686	7.3×10^{-45}
LG16	112	182	188	343	2193	1254	2290	1780	0.654	−0.718	0.209	−0.112	3.0×10^{-44}
LG17	111	168	171	425	2986	1698	3215	2421	0.724	−0.681	0.101	−0.043	5.9×10^{-45}

states lie above the Z pole. The systems of additional Majoranas then mostly have hidden sector eigencontent and have masses close to the mass of the LSP.

We consider now the inclusion of the hidden sector which may have a very significant effect on the relic density. For the case that the Majoranas in the hidden sector are effectively degenerate in mass with the LSP, the LSP can coannihilate with the hidden sector neutralinos generating an enhancement for the density of relic neutralinos relative to that in the MSSM, through the extra degrees of freedom supplied by the hidden sector, so that

$$\Omega_{\tilde{\chi}^0_1} h^2 \simeq f_E \times \Omega^{\rm MSSM}_{\tilde{\chi}^0_1} h^2, \tag{15}$$

where f_E is the relic density enhancement factor given by [22]

$$f_E = \left[1 + \frac{d_{\rm hid}}{d_{\rm vis}}\right]^2, \tag{16}$$

and where $d_{\rm hid}$ is the degree of degeneracy in the hidden sector and $d_{\rm vis}$ is the degree of degeneracy in the visible sector. We note in passing that an analysis on the effects of fields in the hidden sector on the relic density via coannihilation effects was studied in [21] and a similar idea was pursued in [70] but without an additional hidden sector. For the $U(1)^n_X$ extension of the SUGRA model with the hidden sector neutralinos essentially degenerate in mass with the LSP, one has $d_{\rm hid} = 2 \times 2n$, where $2n$ is the number of Majorana fields in the hidden sector with 2 degrees of freedom for each Majorana field. For the case when the neutralino is pure w-ino, the chargino is essentially degenerate in mass with the LSP and in this case $d_{\rm vis} =$ 2(LSP) + 4(chargino), while for the case when the neutralino is a mixture of b-ino, w-ino, and Higgsinos, one has $d_{\rm vis} \to 2$(LSP). Thus, for the case when the neutralino and the chargino are not degenerate as is the case when the eigencontent of the neutralino is a mixture of b-ino, w-ino, and Higgsino, a large f_E can be generated, for example, $f_E = 49$ for $n = 3$, where the maximal f_E we obtain is ∼40 due to coannihilations in the visible sector. We will utilize this enhancement of the relic abundance in fitting the WMAP data.

With the above enhancement mechanism one can achieve a large $\langle \sigma v \rangle_{\rm halo}$ needed for a solution to the PAMELA data and at the same time have a relic density close to the WMAP data. This indeed is the case for models LG16 and LG17 which can explain the PAMELA data via the neutralino annihilation $\tilde{\chi}^0_1 \tilde{\chi}^0_1 \to W^+ W^-$ with the subsequent dominant decay $W^+ \to \ell^+ \nu_\ell$ while at the same time satisfying the relic density constraint via the additional hidden sector degrees of freedom. In these cases, the mixed–w-ino annihilation cross section into $WW \sim 6 \times 10^{-25}$ cm^3 s^{-1}, and only small effects from the possible clumps in the local halo are needed. For LG10, the Higgsino-like LSPs annihilate into both WW and ZZ, where in addition the decay $Z \to \ell^+ \ell^-$ gives a contribution to the positron excess. Here one finds $\langle \sigma v \rangle_{WW+ZZ} \sim 3.5 \times 10^{-25}$ cm^3 s^{-1} and one needs a clump factor of around (2–3) to fit the PAMELA data while the LSP mass is significantly lower, ∼111 GeV [17], than the mixed–w-ino case. Interestingly, this Higgsino-like model produces smaller $\bar{p}$ flux at higher energies and slightly larger flux at lower energies relative to the heavier mixed–w-ino case. Also the Higgsino-like LSP receives less stringent constraints from the Fermi photon line data than the w-ino-like LSP. We note that models with a Higgsino-like LSP have been studied in the past [71]. However, to our knowledge the model class uncovered in [17], for which LG10 is an example, is the first illustration of a SUGRA model with a Higgsino LSP that gives a fit to the PAMELA data.

To elaborate further, the models of Table VII have a neutralino mass in the range of (111–183) GeV which allows a $\langle \sigma v \rangle_{\rm halo}$ in the range $(3.5\text{–}6) \times 10^{-25}$ cm^3 s^{-1}, and, thus, the model can produce the positron excess seen in the PAMELA experiment. Further, as seen in Table VII these models are consistent with the current XENON100 limits and have the possibility to produce scattering cross sections that are discoverable in improved dark matter experiments, i.e., in the range $\sim 5 \times (10^{-45}\text{–}10^{-44})$ cm^2. In addition, these models are consistent with the Fermi-LAT photon data as seen in Table VIII. Hence, the eigencontent of the LSP in these models is mixed–w-ino for LG16 and LG17 and close to being pure Higgsino for LG10, and therefore their dark matter signatures are modified drastically relative to other models classes discussed which are significantly b-ino-like.

In the top panel of Fig. 2 we show several fits to the PAMELA positron fraction where we include the data from recent experiments [32,61]. The analysis of this panel shows general agreement with [13,22,72] for the pure or essentially pure w-ino case (for early work on cosmic rays

TABLE VIII. Top: Predictions for $\tilde{\chi}_1^0\tilde{\chi}_1^0 \to \gamma\gamma$, γZ for the models including the b-ino-like models, Higgsino-like models, and w-ino-like models. Lower: The current experimental constraints from Fermi-LAT [27] on $\gamma\gamma$ and γZ modes are shown with three halo profiles. Constraints are shown for those model classes which can describe the PAMELA data and have large neutralino self-annihilation cross sections into $\gamma\gamma$ and γZ. Shown are the ranges where the models can be constrained where the notation is [...] for the $\gamma\gamma$ mode and (...) is for the γZ mode. All cross sections in the lower table are given in 10^{-27} cm^3 s^{-1}. Models LG16 and LG17 are within reach of the Fermi-LAT limits, as they have a large w-ino content, and are discussed in detail in the text.

Label	E_γ (GeV)	$\langle\sigma v\rangle_{\gamma Z}^{\rm Theory}$ (cm^3/s)	E_γ (GeV)	$\langle\sigma v\rangle_{\gamma\gamma}^{\rm Theory}$ (cm^3/s)
LG1	14	2.7×10^{-30}	53	1.5×10^{-34}
LG2	101	2.6×10^{-30}	118	9.4×10^{-30}
LG3	334	1.7×10^{-32}	340	2.5×10^{-32}
LG4	372	2.2×10^{-34}	377	6.9×10^{-34}
LG5	359	1.1×10^{-33}	365	9.1×10^{-33}
LG6	353	3.2×10^{-32}	359	6.7×10^{-32}
LG7	89	1.2×10^{-28}	108	2.8×10^{-29}
LG8	84	1.5×10^{-28}	104	3.5×10^{-29}
LG9	119	8.8×10^{-29}	135	1.7×10^{-29}
LG10	92	1.8×10^{-28}	111	8.7×10^{-29}
LG11	103	4.0×10^{-29}	121	7.1×10^{-30}
LG12	157	3.5×10^{-29}	169	5.0×10^{-30}
LG13	147	1.3×10^{-31}	160	4.0×10^{-31}
LG14	96	3.1×10^{-30}	114	1.1×10^{-29}
LG15	104	3.1×10^{-30}	121	7.9×10^{-30}
LG16	171	6.0×10^{-27}	182	1.1×10^{-27}
LG17	156	9.4×10^{-27}	168	1.7×10^{-27}

E_γ (GeV)	Navarro-Frenk-White	Einasto	Isothermal	Model $\langle\sigma v\rangle_{(\gamma Z),[\gamma\gamma]}^{\rm theory}$
(90–100) [110–120]	(6.0–3.8) [1.0–1.6]	(4.3–2.8) [0.7–1.1]	(10.3–6.6) [1.7–2.7]	LG10 (0.18) [0.087]
(170–180) [180–190]	(4.0–6.1) [2.7–3.2]	(2.9–4.4) [1.9–2.3]	(6.8–10.4) [4.6–5.5]	LG16 (6.0) [1.1]
(150–160) [160–170]	(8.2–6.3) [2.7–1.7]	(5.9–4.5) [2.0–1.3]	(14.1–10.9) [4.7–3.0]	LG17 (9.4) [1.7]

relevant to this discussion see [73,74]). Here, however, we specifically show that the mixed–w-ino models LG16 and LG17 and the Higgsino LSP model case LG10 provide a good description of the PAMELA data with boosts of the order of unity. For comparison we also show the essentially pure w-ino case, which requires no boost but has difficulty explaining the Fermi photon data. In the lower panel of Fig. 2 we give a comparison of the $\bar{p}$ flux with recently released data [62]. Indeed it is seen that the theoretical prediction of the $\bar{p}$ flux is in good agreement with the data. The boost factors used are rather minimal and are not assumed different for the $\bar{e}$ and $\bar{p}$ fractions, which is in principle a possibility (different boosts are often introduced in order not to upset the $\bar{p}$ flux while enhancing the $\bar{e}$ flux). The analysis we present does not attempt to explain the Advanced Thin Ionization Calorimeter (ATIC) and Fermi high energy $e + \bar{e}$ data. Such data could be explained with an additional electron source [72,75] with a w-ino LSP [25,71,72] or mixed–w-ino LSP [17,22].

IV. SIGNATURE ANALYSIS AT THE LHC AT $\sqrt{s} = 7$ TeV

Signature analyses at center of mass energies of $\sqrt{s} = 10$ TeV and $\sqrt{s} = 14$ TeV at the LHC already exist in the literature, and as mentioned in the introduction, a few analyses at the center of mass energies of $\sqrt{s} = 7$ TeV have also appeared [10–17]. For this analysis, our emphasis is on the discovery of models which admit low mass gluinos in early runs at the LHC consistent with dark matter interpretations for a neutralino LSP.

1. Standard model background.—The discovery of new physics requires an accurate determination of the standard model (SM) background. The recent works of [11,12] have given an analysis of such backgrounds including $2 \to n$ processes at $\sqrt{s} = 7$ TeV appropriate for pp collisions at the LHC. We use for our analysis the simulated SM background of [12] which was generated with MADGRAPH 4.4 [76] for parton level processes, PYTHIA 6.4 [77] for hadronization, and PGS-4 [78] for detector simulation. A MLM matching algorithm with a k_T jet clustering scheme was used to prevent double counting of final states. Further, the b-tagging efficiency in PGS-4 is based on the technical design reports of ATLAS [79] (see [12]), which is similar to the efficiency of CMS [80], with the mistagging rate of the b jet unmodified from the default in PGS-4. In addition TAUOLA is called for tau decays [81]. The processes that are included in the SM background are (QCD 2, 3, 4 jets), ($t\bar{t}$ + 0, 1, 2 jets), ($b\bar{b}$ + 0, 1, 2 jets), ($Z/\gamma(\to l\bar{l}, \nu\bar{\nu})$ + 0, 1, 2, 3 jets), ($W^\pm(\to l\nu)$ + 0, 1, 2, 3 jets), ($Z/\gamma(\to l\bar{l}, \nu\bar{\nu})$ + $t\bar{t}$ + 0, 1, 2 jets), ($Z/\gamma(\to l\bar{l}, \nu\bar{\nu})$ + $b\bar{b}$ + 0, 1, 2 jets), ($W^\pm(\to l\nu)$ + $b\bar{b}$ + 0, 1, 2 jets), ($W^\pm(\to l\nu)$ + $t\bar{t}$ + 0, 1, 2 jets),

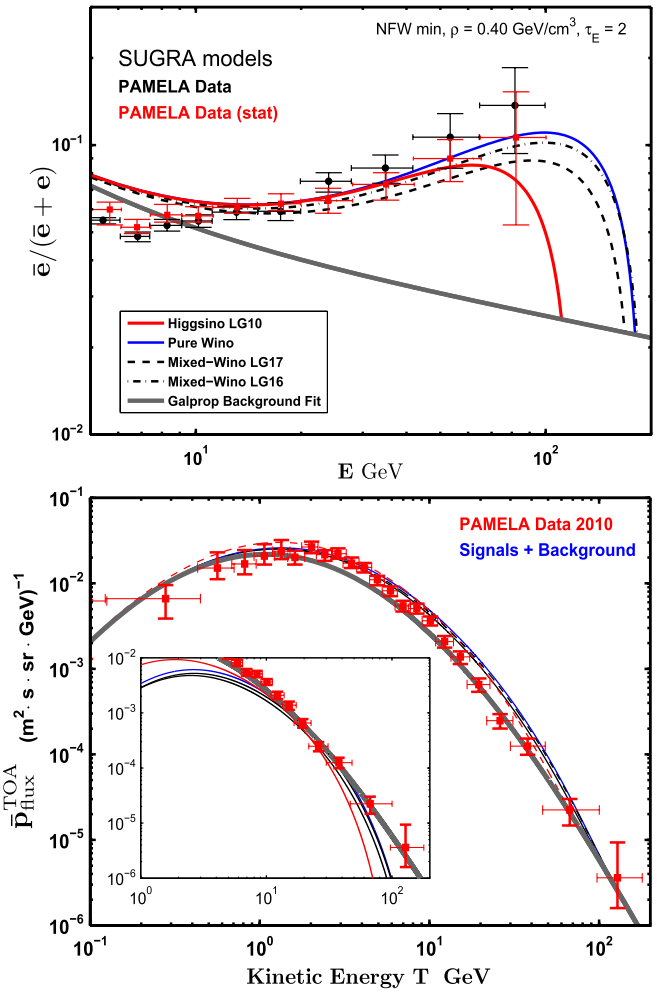

FIG. 2 (color online). Top: Mixed–*w*-ino LSP models LG16 and LG17, the Higgsino LSP model LG10, and the PAMELA positron excess. For comparison a pure *w*-ino LSP model is also shown. Boost factors of (1–3) are used. We note that an LSP with a pure *w*-ino content while compatible with the PAMELA data has difficulties with the $\gamma\gamma$ and γZ cross sections from Fermi monochromatic photon data. For this reason Table I does not contain a pure *w*-ino model. Bottom: The PAMELA antiproton flux and the SUSY models. The $\bar{p}$ flux is compatible with the data. The mixed–*w*-ino models as well as the Higgsino model can produce large LHC jet signatures as discussed in the text.

$(W^{\pm}(\to l\nu) + t\bar{b}(\bar{t}b) + 0, 1, 2\,\text{jets})$, $(t\bar{t}t\bar{t}$, $t\bar{t}b\bar{b}$, $b\bar{b}b\bar{b})$, $(W^{\pm}(\to l\nu) + W^{\pm}(\to l\nu))$, $(W^{\pm}(\to l\nu) + Z(\to \text{all}))$, $(Z(\to \text{all}) + Z(\to \text{all}))$, and $(\gamma + 1, 2, 3\,\text{jets})$. Here l is e, μ, and τ, a jet refers to gluon as well as first- and second-generation quarks, and *all* denotes either l, ν, or jet. The above processes are final state processes at the parton level, i.e., before hadronization. A more detailed discussion of the SM background can be found in [12], which includes a list of cross section, number of events, and luminosity for each process (see Table I of [12]).

2. SUSY signal generation and optimization of signature cuts.—The sparticle spectrum for the signal analysis was generated using SUSPECT [82] via MICROMEGAS [83] and branching ratios are computed with SUSY-HIT [84]. Some differences in the output of the sparticle masses are known to exist when computed with different codes. We have checked our models with SOFTSUSY [85] and found only small differences.

We now discuss a set of signatures used in our early discovery analysis at the LHC at $\sqrt{s} = 7$ TeV. The notation used in the these signatures is as follows: ℓ denotes e and μ, and $p_T(\ell)$ and $p_T(j)$ define the transverse momentum of the lepton ℓ and of the jet j, respectively, while $n(\ell)$ and $n(j)$ give us the number of leptons (ℓ) and the number of jets (j) in the event, respectively. We investigate a large number of cuts on the p_T of jets and leptons in combination with transverse sphericity S_T and missing energy E_T. For clarity, we order objects by their p_T (i.e., the hardest jet would be denoted j_1), and we define m_{eff} and H_T as

$$m_{\text{eff}} = \sum_{i=1}^{4} p_T(j_i) + E_T, \qquad H_T = \sum_{i=1}^{4} p_T(x_i) + E_T, \quad (17)$$

respectively, where x_i is a *visible* object and where the sum is over the first four hardest objects.[3] In this analysis we define a signal that produces S events to be discoverable for a particular signature cut if $S \geq \max\{5\sqrt{B}, 10\}$, where B is the number of SM background events.

In the analysis we investigate a broad set of cuts to enhance the significance. The optimal cuts were found by varying the bounds on observables. First, a broad optimization was carried out where the varied observables include missing energy (100–800 GeV in steps of 50 GeV), transverse sphericity of all visible objects (with a lower bound of 0.15–0.25 in steps of 0.05), number of jets (2–6 in integer steps), and number of b jets (0–3 in integer steps), as well as the p_T of the hardest jet (10–500 GeV in steps of 100 GeV) and second hardest jet (10–250 GeV in steps of 50 GeV). Further, this optimization includes varying the number of jets, the p_T of the hardest jet, p_T of the second hardest jet, and the p_T of all the jets. For the particular cuts, C17 and C18, that deal with opposite sign same flavor (OSSF) leptons, a Z veto is applied; i.e., the leptons invariant mass is not in the 76–105 GeV region. We note that in a preliminary scan, before the large optimization, a variation on cuts for the p_T of leptons was also investigated. However, it was found to be of little use in enhancing the significance at low luminosity for the models we discuss. Given this we omitted cuts on lepton p_T from the large optimization. However, the trileptonic signal is an important signature for the discovery of supersymmetry via the off-shell decay of the W as well as other off-shell processes

[3]One could also define a b jet effective mass to be the sum of the p_Ts of the four hardest b jets. However, accuracy with which p_T of the b jets can be determined may not be high in early runs, and thus the use of b jet effective mass may be experimentally challenging. Several alternate definitions of H_T appear in the literature.

[86]. The trileptonic signal has been considered in the analyses at 7 TeV in recent works [10,11]. A third optimization search was done in this channel by varying transverse sphericity (either no cut or ≥ 0.2), missing energy ($\geq$ 100, 150, 200, 250 GeV), number of jets ($\geq$ 2, 3, 4, 5, 6), $p_T(j_1)$ (no cut or $\geq$ 60, 100, 150 GeV), and $p_T(j_2)$ (no cut or $\geq$ 20, 30, 40, 60, 80, 100 GeV).

A subset of cuts found using the procedure above are listed in Table IX. In choosing these cuts we have taken into account the uncertainty of how well missing energy can be determined in the early runs. For this reason we have taken lower values of $\not{E}_T$, sometimes as low as 100 GeV. Better optimization can occur with other choices, specifically for larger values of $\not{E}_T$. However, this requires a greater degree of confidence on how well $\not{E}_T$ is determined in the early runs.

3. Signature analysis.—Our analysis is carried out to determine the potential for discovery of the dark matter motivated models LG1, …, LG17, for 0.5, 1, 2, and 5 fb^{-1} (with a focus on 1 fb^{-1}) of integrated luminosity with 7 TeV center of mass energy. These models exhibit generic features of a very broad class of SUSY models.

We now discuss Fig. 1, shown in Sec. I, a bit more generally. The potential for discovering the models of Table I at 1 fb^{-1} of integrated luminosity is given in Table X. A subset of the results in Table X is given in Fig. 1. Thus, Table X displays each model's significance $S/\sqrt{B}$ for the 21 cuts listed above. One finds that a particular model, LG$_k$, often has several signatures that lead to large excesses of signal over background, i.e., $S/\sqrt{B} > 5$, and the set of signatures in which the model becomes visible varies significantly from one model to the next. Additionally, in studying the trileptonic channels C20 and C21, we see that consistently only 6 models among those listed in Table I are discoverable (LG1, LG2, LG10, LG11, LG14, and LG15) and the majority of the other models show fewer than 10 events in the trileptonic channels.

The overall production cross section of superparticles is determined mainly by the production of squarks and gluinos. For the gluino production modes at the LHC, the cross section is determined by the gluino mass. However, for models with low mass gluinos, like those that appear in Table I, the detectable signals at the LHC are strongly influenced by the other low-lying superparticles, i.e., the superparticles that are lighter than the gluino. In Fig. 3, an analysis of the jet multiplicity and the transverse momentum of the leading jets is given for LG3, LG4, LG11, LG13, and LG14. The distributions for jet multiplicity and jet momentum look quite different from model to model. For instance, the model LG11 has a gluino mass of 433 GeV, and several of its superparticles are lighter than the gluino, including the lighter stop and gauginos. This leads to lengthy cascade decay chains which produce multiple jets. Further, the mass differences between the superparticles in LG11 are relatively large which gives rise to large momentum of the SM final states including jets. In contrast, models LG3 and LG4 tend to produce events with less jet multiplicity and smaller transverse momentum, which is due to the fact that these models having a gluino

TABLE IX. A table of cuts that are used for the analysis. Cuts C17 and C18 have a Z veto applied, and in these cuts the subscripts a and b indicate that they may be different flavors. The Z veto is applied only to OSSF. In addition cuts C2–C19 have $S_T \geq 0.2$.

C1	$\not{E}_T \geq 100$ GeV	⋯	⋯
C2	$\not{E}_T \geq 100$ GeV	⋯	⋯
C3	$\not{E}_T \geq 100$ GeV	$n(\ell) = 0$	$p_T(j_1) \geq 150$ GeV, $p_T(j_2, j_3, j_4) \geq 40$ GeV
C4	$\not{E}_T \geq 250$ GeV	$n(\ell) = 0$	$p_T(j_1) \geq 250$ GeV, $p_T(j_2, j_3, j_4) \geq 40$ GeV
C5	$\not{E}_T \geq 150$ GeV	$n(\ell) = 0$	$p_T(j_1) \geq 150$ GeV, $p_T(j_2, j_3, j_4) \geq 40$ GeV
C6	$\not{E}_T \geq 250$ GeV	$n(\ell) = 0$	$p_T(j_1) \geq 100$ GeV, $p_T(j_2) \geq 40$ GeV
C7	$\not{E}_T \geq 200$ GeV	$n(\ell) = 0$	$p_T(j_1) \geq 30$ GeV
C8	$\not{E}_T \geq 200$ GeV	$n(j) \geq 2$, $n(\ell) \geq 2$	⋯
C9	$\not{E}_T \geq 200$ GeV	$n(b \text{ jets}) = 1$	⋯
C10	$\not{E}_T \geq 100$ GeV	$n(\ell) = 0$, $n(b \text{ jets}) \geq 1$	⋯
C11	$\not{E}_T \geq 100$ GeV	$n(\ell) = 0$, $n(b \text{ jets}) \geq 2$	⋯
C12	$\not{E}_T \geq 100$ GeV	$n(j) \geq 4$	⋯
C13	$\not{E}_T \geq 100$ GeV	$n(j) \geq 4$	$p_T(j_1) \geq 100$ GeV, $m_{\text{eff}} \geq 400$ GeV
C14	$\not{E}_T \geq 100$ GeV	$n(j) \geq 4$	$p_T(j_1) \geq 100$ GeV, $m_{\text{eff}} \geq 550$ GeV
C15	$\not{E}_T \geq 100$ GeV	$n(j) + n(\ell) \geq 4$	$p_T(j_1) \geq 100$ GeV, $H_T \geq 400$ GeV
C16	$\not{E}_T \geq 100$ GeV	$n(j) + n(\ell) \geq 4$	$p_T(j_1) \geq 100$ GeV, $H_T \geq 550$ GeV
C17	$\not{E}_T \geq 100$ GeV	$n(\ell_a^+) = 1$, $n(\ell_b^-) = 1$	$p_T(\ell_2) \geq 20$ GeV, $p_T(j_1) \geq 100$ GeV, $p_T(j_2) \geq 40$ GeV
C18	$\not{E}_T \geq 100$ GeV	$n(\ell_a^+) = 1$, $n(\ell_b^-) = 1$	$p_T(\ell_2) \geq 20$ GeV, $p_T(j_2) \geq 40$ GeV
C19	$\not{E}_T \geq 100$ GeV	$n(j) \geq 4$	$p_T(j_1) \geq 100$ GeV, $\not{E}_T \geq 0.2 m_{\text{eff}}$
C20	$\not{E}_T \geq 100$ GeV	$n(\ell) = 3$, $n(j) \geq 2$	$p_T(j_1) \geq 150$ GeV
C21	$\not{E}_T \geq 150$ GeV	$n(\ell) = 3$	$p_T(j_2) \geq 40$ GeV

TABLE X. A display of the signal significance $S/\sqrt{B}$ in each discovery channel for the models in Table I for 1 fb^{-1} of integrated luminosity at the LHC. As already mentioned in Sec. IV for a signal to be discoverable we require $S \geq \max\{5\sqrt{B}, 10\}$.

	C1	C2	C3	C4	C5	C6	C7	C8	C9	C10	C11	C12	C13	C14	C15	C16	C17	C18	C19	C20	C21
LG1	6	9	18	6	19	4	5	3	7	10	8	13	17	20	16	19	2	2	17	3	2
LG2	3	4	4	13	7	14	9	10	5	2	2	4	5	8	6	8	1	1	4	9	10
LG3	4	3	1	3	2	8	7	0	2	3	1	4	3	2	2	2	0	0	1	0	0
LG4	4	2	0	1	1	5	7	0	1	0	0	1	1	1	1	1	0	0	0	0	0
LG5	4	2	0	1	1	5	6	0	1	1	0	2	1	1	1	1	0	0	0	0	0
LG6	4	3	1	3	2	8	8	0	1	1	0	3	2	2	2	2	0	0	1	0	0
LG7	6	9	17	9	23	9	9	2	12	12	11	13	17	20	16	19	0	0	17	0	0
LG8	7	10	18	9	24	9	10	2	11	13	10	15	20	21	19	21	0	1	18	1	1
LG9	0	0	1	2	1	1	1	1	1	0	0	0	1	1	1	1	0	0	1	0	0
LG10	18	24	18	13	25	29	31	4	21	23	16	30	33	28	31	27	0	0	19	1	4
LG11	12	19	31	24	39	17	15	16	24	33	42	27	34	38	32	36	2	5	34	9	5
LG12	2	4	10	16	16	8	6	3	8	6	7	6	8	11	7	10	0	1	10	2	2
LG13	6	5	8	25	14	17	13	0	11	6	5	7	7	9	7	9	0	0	7	0	0
LG14	8	10	10	24	17	31	19	25	17	6	5	11	15	20	15	20	4	5	12	20	20
LG15	9	11	16	38	26	34	22	22	19	8	7	13	18	24	18	25	5	5	16	20	18
LG16	19	28	15	11	18	11	14	0	11	27	15	37	27	16	25	15	0	0	17	0	0
LG17	7	10	13	7	19	10	11	0	11	11	8	14	17	16	16	15	0	0	14	0	0

as the NLSP; i.e., these models are GNLSPs. For these GNLSP models the masses of the gluino and the LSP are correlated in the gluino coannihilation mechanism such that the mass gap is relatively small.

Specifically, LG3 has $M_{\tilde{g}} - M_{\tilde{\chi}_1^0} \sim 50$ GeV and the gluino production is, overwhelmingly, the dominant production mode. For this model, the gluinos decay directly to the LSP + 2 jets, i.e., $\mathcal{B}r(\tilde{g} \to (b\bar{b}\tilde{\chi}_1^0, q\bar{q}\tilde{\chi}_1^0)) \sim (20, 80)\%$, where q stands for the first two-generation quarks. We note in passing that generally one needs to take into account the radiative decay of the gluino, $\tilde{g} \to g\tilde{\chi}_1^0$. Such a case occurs, for example, in LG4, and the decay $\tilde{g} \to g\tilde{\chi}_1^0$ dominates the branching ratio. The relatively small mass splitting in model LG3 between the gluino and the LSP (as well as the extreme case of LG4) makes this model class harder to discover due to the softer jets and low jet multiplicity, compared to other models. (For recent work on relatively small gluino-LSP splittings see [2,3,15,50,52].) This feature is illustrated further in Tables X and XI. We note that in such cases where the mass gap between gluino and the LSP is extremely small, the effects of the initial state radiation can be substantial for the collider signatures. We also note that although it can be challenging to discover events from gluino production for the GNLSP models (depending on the degree of the mass degeneracy), one should keep in mind that some other subdominant SUSY production modes could be detectable and become the leading signals for such models. For example, in model LG3, the stop is relatively light and decays entirely into a chargino and bottom quark, i.e., $\mathcal{B}r(\tilde{t}_1 \to \tilde{\chi}_1^+ b) \sim 100\%$, and the chargino subsequently decays entirely into a neutralino and a W boson, i.e., $\mathcal{B}r(\tilde{\chi}_1^+ \to \tilde{\chi}_1^0 W^+) \sim 100\%$. Hence, this GNLSP model class may be able to produce discoverable leptonic events through these decay chains with upgraded center of mass energy and luminosity.

Further, these features of the GNLSP models can explicitly be seen by studying the top panels of Fig. 3 and by observing the relative broadness (or width) of the p_T distribution of models LG11 and LG14 relative to LG3 and LG4. In addition, LG13, a stop NLSP model, is also peaked at low jet p_T much like LG3 and LG4. The stop mass for model LG13 is near 200 GeV and the stop-LSP mass splitting is small ($\lesssim 30$ GeV). Thus, this model produces stops at a large rate, which decay [via an off-shell loop-induced and flavor changing neutral-current (FCNC) decay] into a charm quark and LSP ($\tilde{t}_1 \to c\tilde{\chi}_1^0$) with a $\sim$75% branching ratio. However, the softness of jets in LG13 mimics the softness of jets in LG4 in part due to the phase space, which explains the peaking of the distributions at low p_T. The restricted phase space from the small mass splittings is also why the effective mass distribution for stop NLSPs is narrow (see [3]) relative to other cases.

In Fig. 4 we highlight the GNLSP model LG3, which satisfies the double-sided relic density band, along with the light stau and stop models, LG2 and LG13, which also satisfy the WMAP bound via scalar coannihilations. Thus, Fig. 4 shows jet p_T, signal plus background, for the models LG2, LG3, and LG13 compared to the SM background alone. As discussed earlier the model LG3 arises from gluino coannihilations and has a relatively small mass splitting between the gluino and the LSP neutralino. This is to be contrasted with the model LG2, which satisfies the WMAP relic density band via stau coannihilations, or the model LG13, which also satisfies the WMAP relic density band via stop coannihilations. Because of the compressed spectra of LG2 and LG13, there are more jets arising from

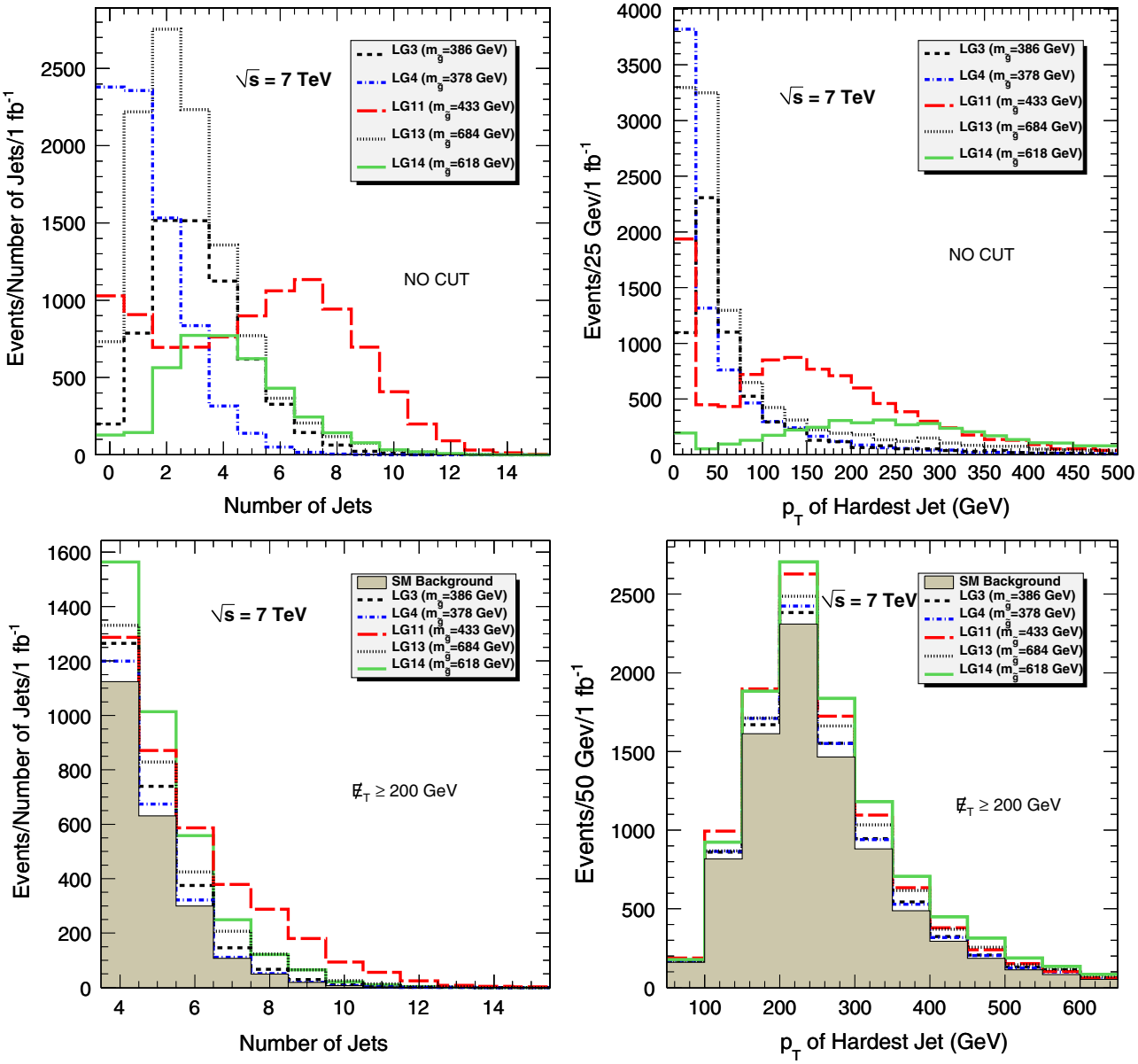

FIG. 3 (color online). Top left: Distribution of the number of jets without cuts. Top right: Distribution of the p_T of the hardest jet also without cuts. Bottom left: Distribution of the number of SUSY events (plus SM background) vs the number of jets after a cut of $E_T \geq 200$ GeV. Bottom right: Distribution of the number of SUSY events (plus SM background) vs the p_T of the hardest jet after a cut of $E_T \geq 200$ GeV.

the combinations of both low mass gluino and the low mass squark production relative to the dominant gluino production found in the GNLSP model LG3. This effect is exhibited in the figure. For model LG2, as the scalars are quite light, and even lighter than the 715 GeV gluino, the cross section for the production of squarks as well as the mixed squark gluino production cross sections are about an order of magnitude larger than the $\tilde{g}\,\tilde{g}$ production. Here the gluino two-body decay modes are spread out rather uniformly with no dominant channel. Instead the first two-generation squark decay modes are short with large branchings. In particular, one has for the first two-generation squarks $\mathcal{B}r(\tilde{q}_R \to \tilde{\chi}_1^0 q) \sim 100\%$ and $\mathcal{B}r(\tilde{q}_L \to \tilde{\chi}_2^0 q) \sim 32\%$ as well as $\mathcal{B}r((\tilde{q}_{d_L}, \tilde{q}_{u_L}) \to \tilde{\chi}_1^{(-,+)}(q_u, q_d)) \sim (60\text{–}65)\%$ for each decay. Thus, the two-body decays of the first two-generation squarks provide the large signal in model LG2 even though the gluino is quite light. In addition, for LG2, the direct production of chargino pairs as well as chargino and neutralino production is competitive with the squark production, leading to leptonic decays and large lepton multiplicities. The discovery potential of the models is also exhibited in Fig. 1, where one finds that the significance of LG3 and LG4 is much less than for LG11.

In Fig. 5 (left panel) we show the potential for early discovery for the PAMELA compliant model class

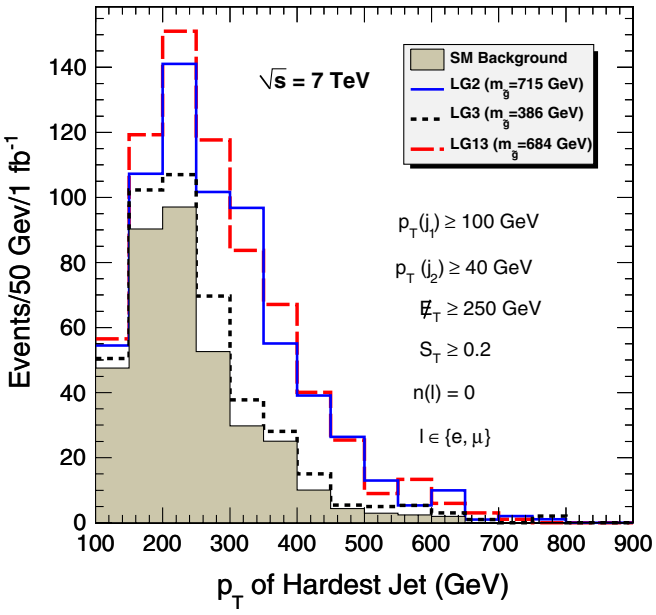

FIG. 4 (color online). SUSY plus SM background events vs $p_T(j_1)$ at 1 fb^{-1} for the signature cut $p_T(j_1) \geq 100$ GeV, $p_T(j_2) \geq 40$ GeV, $E_T \geq 250$ GeV, $S_T \geq 0.2$, and $n(\ell) = 0$ for LG2, LG3, and LG13. The figure illustrates the softness of the jets in model LG3, a GNLSP model, relative to the models LG2 and LG13.

discussed in Table VII at $\sqrt{s} = 7$ TeV and at an integrated luminosity of 1 fb^{-1}. The displayed models have a rather large gluino production. Since the gluino, the light chargino, and the second-heaviest neutralino are the lightest SUSY particles beyond the LSP, and the squarks are rather heavy for these models, the sparticle production at the LHC will be dominated by $\tilde{g}\,\tilde{g}$, $\tilde{\chi}_2^0\tilde{\chi}_1^{\pm}$, and $\chi_1^+\chi_1^-$ production. For example, models (LG10, LG16, LG17) have a total SUSY cross section of $\sim$(12, 15, 5) pb at leading order and the gluino production is at the level of $\sim$(9, 14, 4) pb, respectively. The chargino neutralino production makes up most of the remaining part of the cross section. The leading decays of the gluino are $\tilde{g} \to \tilde{\chi}_1^{\pm} + \bar{q}q'$ and $\tilde{g} \to \tilde{\chi}_2^0/\tilde{\chi}_1^0 + q\bar{q}$. These decays are subsequently followed by $\tilde{\chi}_2^0 \to \tilde{\chi}_1^0 + \bar{f}f$ and $\tilde{\chi}_1^{\pm} \to \tilde{\chi}_1^0 + \bar{f}f'$, where f and f' are the standard model quarks and leptons, respectively. In particular, the lightness of the gluino in the three models (LG10, LG16, and LG17) gives rise to multijets which produce a strong signal over the background. Hence, these models are good candidates for early discovery. Further, if a model of the type LG10, LG16, or LG17 is verified at the LHC, it would also provide a consistent explanation of the PAMELA anomaly. However, to fully demonstrate the validity of the models, additional luminosity would be needed to extract information about the neutralino mass. We do not give a detailed methodology for accomplishing this, but as argued in [13] it may be possible to extract information about the neutralino and the chargino states in the gluino decay products.

In Fig. 6, we show a comparison of dijet invariant mass distributions for the GNNLSP models compared to models where the gluino is positioned higher in the mass hierarchy. One sees the GNNLSP models (LG7, LG8, and LG10)

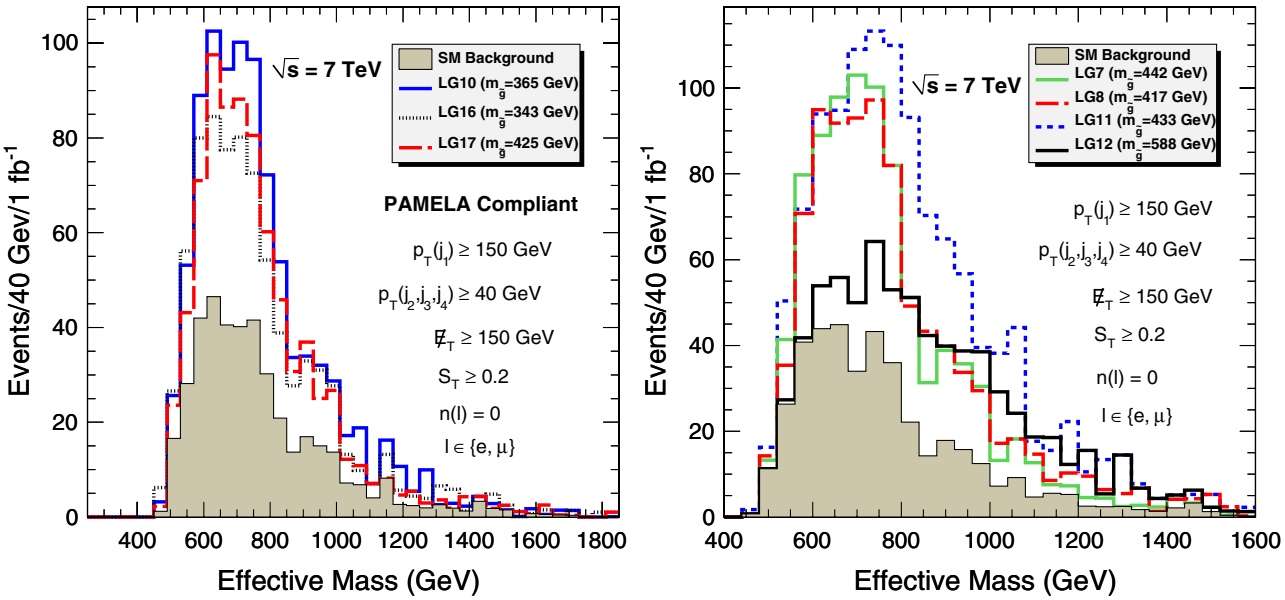

FIG. 5 (color online). Left: SUSY plus SM background events vs m_{eff} at 1 fb^{-1} of integrated luminosity for the signature cut $p_T(j_1) \geq 150$ GeV, $p_T(j_2, j_3, j_4) \geq 40$ GeV, $E_T \geq 150$ GeV, $S_T \geq 0.2$, and $n(\ell) = 0$ for the PAMELA compliant models. As discussed in the text LG10 is a Higgsino LSP model and LG16 and LG17 are models with a mixed–w-ino LSP. Right: The same as the left panel except for a subset of the GNNLSP models (with chargino and neutralino degenerate), i.e., LG7 and LG8, along with the compressed models LG11 and LG12, which in addition to a low mass gluino also have a light stau and a light stop and have a compressed mass spectrum for the first two-generation squarks and sleptons.

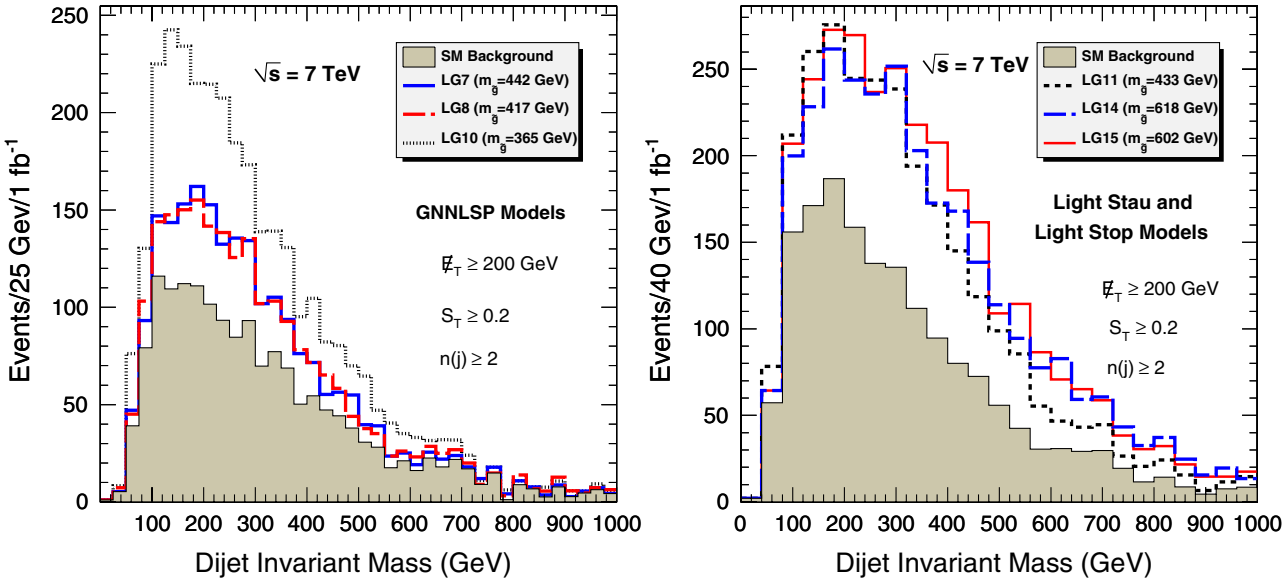

FIG. 6 (color online). Left: SUSY plus SM background events vs the dijet invariant mass (m_{jj}) at 1 fb^{-1} of integrated luminosity for signature cut $E_T \geq 200$ GeV, $S_T \geq 0.2$, and $n(j) \geq 2$ for the models LG7, LG8, and LG10. Right: The same as the left plot except that the analysis is for models LG11, LG14, and LG15. The left panel shows the light gluino models which are effectively GNNLSP models, while the right panel shows the models with a compressed mass spectrum for the scalars and for the light gluinos. As such, the right panel shows distributions which are significantly broader from the squark production and decays.

have a relatively narrow dijet invariant mass which arises from these models being dominated by the three-body decays resulting from $\tilde{\chi}_2^0\tilde{\chi}_1^{\pm}$, $\tilde{\chi}_1^+\tilde{\chi}_1^-$, and $\tilde{g}\,\tilde{g}$ production. Further, the distributions for the models LG8 and LG10 become depleted (or more narrow) relative to the light stau and light stop models from the three-body decays which result in softer jets. These subsequent decays produce an increase in the multijet signal compared to the SM background. However, the light stau and light stop models LG11, LG14, and LG15 have a relatively broader distribution, which arises from the compression of their sparticle spectrum. For these models, all the sparticle masses are below 700 GeV. Further, LG14 and LG15, where the mass spectra are compressed, the gluino is in the 31st position of the mass hierarchy. The compressed spectra causes a large sampling of sparticle production, which results in a production of many jets with a more diverse range of momentum.

The right panel of Fig. 7 shows the number of SUSY signature events plus the SM background in 40 GeV energy bins at 1 fb^{-1} of integrated luminosity vs the dijet invariant mass for models LG1, LG11, and LG14. As exhibited in this figure, these models have a significantly larger dijet invariant mass compared to the SM. As discussed earlier LG11 has a relatively large sparticle mass splitting in the scalar sector relative to the LSP mass as well as lengthy cascade decay chains that produce multiple final state jets with large momentum. Further, the right panel of Fig. 7 helps illustrate the effectiveness of the m_{eff} cut. Comparing the values of C13 to C14 in Table X, one sees that the significance for models LG1, LG11, and LG14 increases as m_{eff} increases. For the case when $m_{\text{eff}} \geq 400$ GeV (C13) we get $S/\sqrt{B} = (17, 34, 15)$ and when $m_{\text{eff}} \geq 550$ GeV (C14) we get $S/\sqrt{B} = (20, 38, 20)$, respectively, for (LG1, LG11, LG14). However, models LG3, LG10, and LG16 have a reverse effect, i.e., $S/\sqrt{B} = (3, 23, 27)$ for $m_{\text{eff}} \geq 400$ GeV (C13) and $S/\sqrt{B} = (2, 15, 15)$ for $m_{\text{eff}} \geq 550$ GeV (C14) for (LG3, LG10, LG16), respectively. These effects arise since models LG3, LG10, and LG16 have lower jet multiplicity, less missing energy, and fewer cascades than the models shown in the right panel of Fig. 7. For instance, the model LG16 cross section is dominated by $\tilde{g}\,\tilde{g}$ production with the $\tilde{g}$ dominantly decaying into $\tilde{\chi}_1^0$ or $\tilde{\chi}_1^{\pm}$. This results in low jet multiplicity and lower missing energy compared to models LG1, LG11, and LG14.

4. Mass reconstruction.—We now discuss the potential to do mass reconstruction for some of the models with the early data. In the left panel of Fig. 7 we display the number of SUSY signature events plus background events in 20 GeV energy bins at 1 fb^{-1} of integrated luminosity vs the OSSF dilepton invariant mass for models LG11, LG14, and LG15. The plot also displays the cuts used as well as the standard model background alone for comparison. In large portions of the figure, the SUSY signals plus the background distribution stand significantly above the background. The leptonic events are mostly produced from the gaugino cascade decays through low-lying sleptons. If the OSSF dileptons arise from the same decay chain $\tilde{\chi}_2^0 \rightarrow \tilde{\ell}^{\pm}\ell^{\mp} \rightarrow \tilde{\chi}_1^0\ell^{\pm}\ell^{\mp}$, the invariant mass from the reconstruction of the dileptons obeys the following mass relations for on-shell sleptons:

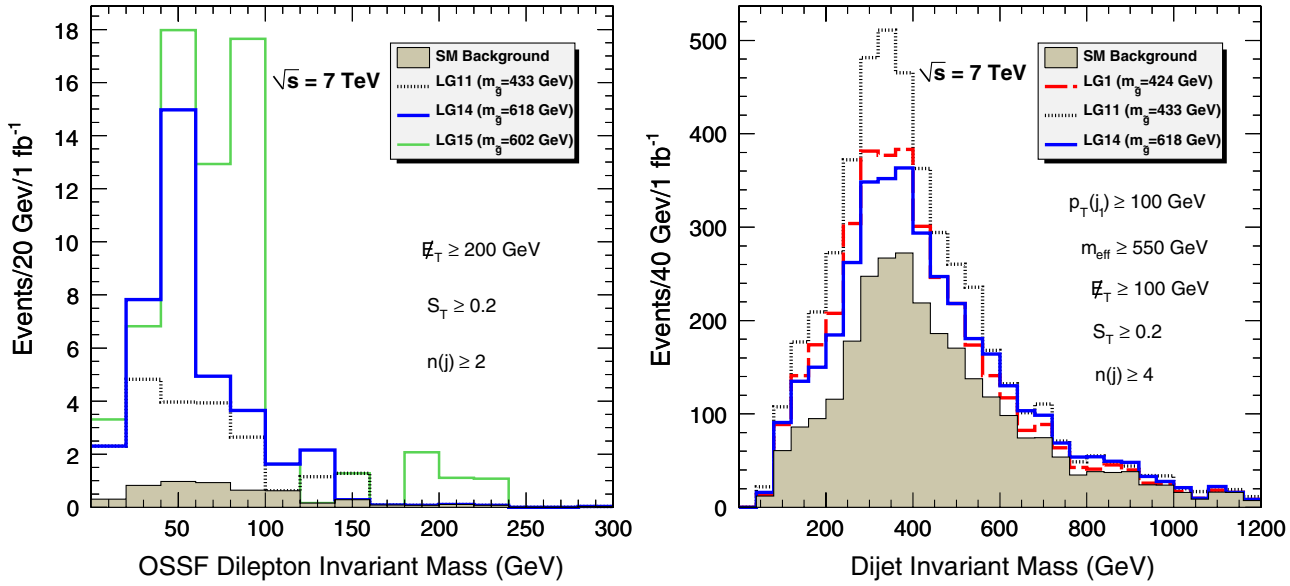

FIG. 7 (color online). Left: SUSY plus background events for models LG11, LG14, and LG15 vs the OSSF dilepton invariant mass ($m_{\ell^+\ell^-}$) at 1 fb^{-1} for signature cut $E_T \geq 200$ GeV, $S_T \geq 0.2$, and $n(j) \geq 2$ with 2 leptons of any sign and flavor. Right: SUSY plus background events for models LG1, LG11, and LG14 vs the dijet invariant mass (m_{jj}) at 1 fb^{-1} of integrated luminosity for signature cut $E_T \geq 100$ GeV, $S_T \geq 0.2$, $p_T(j_1) \geq 100$ GeV, $m_{\rm eff} \geq 550$ GeV, and $n(j) \geq 4$. Here the peak in the distribution is a consequence of the $m_{\rm eff}$ cut.

$$M_{\ell^+\ell^-} \leq M_{\tilde{\chi}_2^0}\sqrt{1-\frac{M_{\tilde{\ell}}^2}{M_{\tilde{\chi}_2^0}^2}}\sqrt{1-\frac{M_{\tilde{\chi}_1^0}^2}{M_{\tilde{\ell}}^2}}. \tag{18}$$

In particular, for model LG15 the three sleptons, $(\tilde{\tau}_1, \tilde{e}_R, \tilde{\mu}_R)$ with the latter two being degenerate, contribute to the OSSF dilepton events with the dilepton invariant mass lying between $\tilde{\chi}_1^0$ and $\tilde{\chi}_2^0$. Using the sparticle masses from LG15, i.e., $(M_{\tilde{\chi}_1^0}, M_{\tilde{\ell}_R}, M_{\tilde{\chi}_2^0}) = (121, 137, 240)$ GeV, one can use Eq. (18) to obtain $M_{\ell^+\ell^-} \lesssim 92$ GeV from the $\tilde{e}_R/\tilde{\mu}_R$ decay modes. The $\tilde{\chi}_2^0$ decays into $\tilde{\chi}_1^0$ via $\mathcal{B}r(\tilde{\chi}_2^0 \to \tilde{\ell}_R^{\pm}\ell^{\mp}) \simeq 28\%$, and then the right-handed slepton decays entirely into a lepton and $\tilde{\chi}_1^0$, i.e., $\mathcal{B}r(\tilde{\ell}_R^{\pm} \to \tilde{\chi}_1^0\ell^{\pm}) \simeq 100\%$. The decay of the light stau follows similarly through $\mathcal{B}r(\tilde{\chi}_2^0 \to \tilde{\tau}_1^{\pm}\tau^{\mp}) \simeq 33\%$, and then the stau decays entirely into $\tilde{\chi}_1^0$ and a τ, i.e., $\mathcal{B}r(\tilde{\tau}_1^{\pm} \to \tilde{\chi}_1^0\tau^{\pm}) \simeq 100\%$. The tau produced from the $\tilde{\chi}_2^0$ decay has a subsequent leptonic tau decay with branching ratio of $\mathcal{B}r(\tau \to \ell\nu_\ell\nu_\tau) \simeq 35\%$. We do not attempt to reconstruct taus here, and we note that there are also further mixings arising from chargino decays which require flavor subtraction and other techniques to isolate the lepton pairs coming from the same cascade decay. Further, due to the low statistics at the early runs of the LHC data, we do not perform a more detailed mass reconstruction in our analysis here. As discussed above, and as can be seen in Fig. 7, the mixings arising from other processes are rather small and the edge in the dilepton invariant mass agrees well with the prediction of Eq. (18).

We now discuss the reconstruction of the b-tagged dijet invariant mass peak. In the left panel of Fig. 8 we give an analysis of the number of SUSY event vs the b-tagged dijet invariant mass (m_{bb}) at 1 fb^{-1} for the models LG1, LG7, and LG8 for the cuts displayed as well as a comparison to the SM background. One finds that the three models are distinguishable above the background. For these models, the majority of the b-tagged dijet events come from the gluino off-shell decay $\tilde{g} \to \tilde{\chi}_2^0 + b\bar{b}$, which leads to an upper bound of the kinematic end point $M_{bb} \leq M_{\tilde{g}} - M_{\tilde{\chi}_2^0}$ that is estimated to be in the range (300–322) GeV. In the left panel of Fig. 8, one sees a hint of an end point forming in this region. However, for these models, the kinematic end point is not yet discernible; more luminosity would be needed, and further, additional uncertainties arise in the interpretation of the invariant mass due to additional cascade processes. A similar analysis can be given for models LG11, LG14, and LG15 in the right panel of Fig. 8. The source of the jets for the three models differ from those of the left panel of Fig. 8 due to their spectra. Further, LG11 produces a significantly larger number of jet events compared to those for LG14 and LG15 due to its light color particles, i.e., the gluino and the stop, dominantly decaying to b jet final states. In addition, some of the b jets in the models from Fig. 8 come from the light CP even Higgs. For example, in model LG15 $\mathcal{B}r(\tilde{\chi}_2^0 \to \tilde{\chi}_1^0 h) \sim 30\%$ and $\mathcal{B}r(h \to b\bar{b}) \sim 80\%$. Thus with increased statistics one may be able to partially reconstruct events coming from the Higgs decay in this model and other models as well.

More generally in Table XI we summarize the result of our analysis for the full set of integrated luminosities

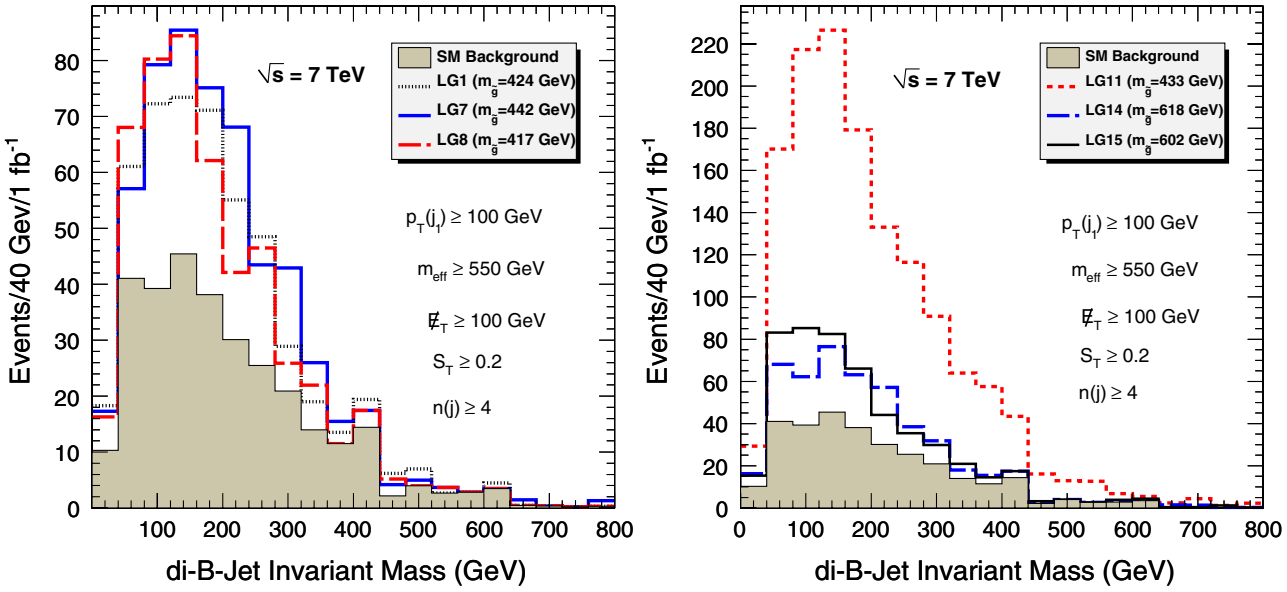

FIG. 8 (color online). Left: SUSY plus SM background events vs the b-tagged dijet invariant mass (m_{bb}) at 1 fb^{-1} of integrated luminosity for signature cut $E_T \geq 100$ GeV, $S_T \geq 0.2$, $p_T(j_1) \geq 100$ GeV, $m_{\text{eff}} \geq 550$ GeV, and $n(j) \geq 4$ for the models LG1, LG7, and LG8. Right: The same as the left panel except that the analysis is for models LG11, LG14, and LG15. As discussed in the text, there is a hint of kinematical edges forming for some of the models in the di-b jet invariant mass plots exhibited above.

0.5, 1, 2, and 5 fb^{-1}. The entries in the boxes in this table indicate the integrated luminosity at which a model listed in the first column will become visible in a specific signature channel listed in the top row. Thus, the entries in Table XI show that a good number of the models in Table I will become visible at 0.5 fb^{-1} of integrated luminosity, and all of the models given in Table I will become visible (in at least one channel) at 5 fb^{-1} of integrated luminosity. Indeed, as discussed above, one observes that the relative mass splitting and the relative position of the gluino within the sparticle mass hierarchies strongly influence the discovery capability of the LG models. Several channels in some cases are needed to establish a signal, and the variance among channels for different models is apparent.

TABLE XI. The values in the table are the integrated luminosity in units of fb^{-1} when the model is first discoverable in that channel. The table shows that many of the low mass gluino models will become visible with an integrated luminosity of 0.5 fb^{-1}, and all models become visible with an integrated luminosity of 2 fb^{-1} except the model LG9, which requires an integrated luminosity of 5 fb^{-1} to be discovered under the criterion given in Sec. IV and in the caption of Table X. $\cdots$ means that the models do not produce the needed significance to be discovered with up to 5 fb^{-1} at $\sqrt{s} = 7$ TeV.

	C1	C2	C3	C4	C5	C6	C7	C8	C9	C10	C11	C12	C13	C14	C15	C16	C17	C18	C19	C20	C21
LG1	1.0	0.5	0.5	1.0	0.5	2.0	1.0	5.0	0.5	0.5	0.5	0.5	0.5	0.5	0.5	0.5	$\cdots$	$\cdots$	0.5	5.0	$\cdots$
LG2	5.0	2.0	2.0	0.5	1.0	0.5	0.5	0.5	1.0	$\cdots$	$\cdots$	2.0	1.0	0.5	1.0	0.5	$\cdots$	$\cdots$	2.0	2.0	1.0
LG3	2.0	5.0	$\cdots$	5.0	5.0	0.5	1.0	$\cdots$	$\cdots$	5.0	$\cdots$	2.0	5.0	$\cdots$	5.0	$\cdots$	$\cdots$	$\cdots$	$\cdots$	$\cdots$	$\cdots$
LG4	2.0	$\cdots$	$\cdots$	$\cdots$	$\cdots$	2.0	1.0	$\cdots$	$\cdots$	$\cdots$	$\cdots$	$\cdots$	$\cdots$	$\cdots$	$\cdots$	$\cdots$	$\cdots$	$\cdots$	$\cdots$	$\cdots$	$\cdots$
LG5	5.0	$\cdots$	$\cdots$	$\cdots$	$\cdots$	2.0	1.0	$\cdots$	$\cdots$	$\cdots$	$\cdots$	$\cdots$	$\cdots$	$\cdots$	$\cdots$	$\cdots$	$\cdots$	$\cdots$	$\cdots$	$\cdots$	$\cdots$
LG6	2.0	5.0	$\cdots$	5.0	$\cdots$	0.5	0.5	$\cdots$	$\cdots$	$\cdots$	$\cdots$	5.0	$\cdots$	$\cdots$	$\cdots$	$\cdots$	$\cdots$	$\cdots$	$\cdots$	$\cdots$	$\cdots$
LG7	1.0	0.5	0.5	0.5	0.5	0.5	0.5	$\cdots$	0.5	0.5	0.5	0.5	0.5	0.5	0.5	0.5	$\cdots$	$\cdots$	0.5	$\cdots$	$\cdots$
LG8	1.0	0.5	0.5	0.5	0.5	0.5	0.5	$\cdots$	0.5	0.5	0.5	0.5	0.5	0.5	0.5	0.5	$\cdots$	$\cdots$	0.5	$\cdots$	$\cdots$
LG9	$\cdots$	$\cdots$	$\cdots$	5.0	$\cdots$	$\cdots$	$\cdots$	$\cdots$	$\cdots$	$\cdots$	$\cdots$	$\cdots$	$\cdots$	$\cdots$	$\cdots$	$\cdots$	$\cdots$	$\cdots$	$\cdots$	$\cdots$	$\cdots$
LG10	0.5	0.5	0.5	0.5	0.5	0.5	0.5	2.0	0.5	0.5	0.5	0.5	0.5	0.5	0.5	0.5	$\cdots$	$\cdots$	0.5	$\cdots$	5.0
LG11	0.5	0.5	0.5	0.5	0.5	0.5	0.5	0.5	0.5	0.5	0.5	0.5	0.5	0.5	0.5	0.5	5.0	2.0	0.5	2.0	2.0
LG12	5.0	2.0	0.5	0.5	0.5	0.5	1.0	5.0	0.5	1.0	1.0	1.0	0.5	0.5	0.5	0.5	$\cdots$	$\cdots$	0.5	$\cdots$	$\cdots$
LG13	1.0	1.0	0.5	0.5	0.5	0.5	0.5	$\cdots$	0.5	1.0	2.0	1.0	0.5	0.5	1.0	0.5	$\cdots$	$\cdots$	0.5	$\cdots$	$\cdots$
LG14	0.5	0.5	0.5	0.5	0.5	0.5	0.5	0.5	0.5	1.0	2.0	0.5	0.5	0.5	0.5	0.5	2.0	1.0	0.5	0.5	0.5
LG15	0.5	0.5	0.5	0.5	0.5	0.5	0.5	0.5	0.5	0.5	1.0	0.5	0.5	0.5	0.5	0.5	2.0	1.0	0.5	0.5	1.0
LG16	0.5	0.5	0.5	0.5	0.5	0.5	0.5	$\cdots$	0.5	0.5	0.5	0.5	0.5	0.5	0.5	0.5	$\cdots$	$\cdots$	0.5	$\cdots$	$\cdots$
LG17	1.0	0.5	0.5	0.5	0.5	0.5	0.5	$\cdots$	0.5	0.5	0.5	0.5	0.5	0.5	0.5	0.5	$\cdots$	$\cdots$	0.5	$\cdots$	$\cdots$

V. CONCLUSION

In this work we discussed the sparticle landscape in the context of a low mass gluino which is one of the prime superparticles that has the potential of being produced as well as detected at the early runs of the LHC. This is due to the gluino (and also squarks) being strongly interacting and typically having the largest production cross section in pp collisions at the LHC for sufficiently low gluino masses. The low mass gluino models considered arise in a variety of settings including mSUGRA, nonuniversal SUGRA models, and in supergravity and string models with a very weakly coupled $U(1)^n$ extended hidden sector. A number of specific benchmark models were analyzed and found to be encouraging for discovery at both the LHC and in dark matter experiments. It is found that the eigencontent of the LSP in such models can vary over a wide range from the LSP being a pure b-ino or a mixed w-ino (LG16 and LG17) to the LSP being heavily Higgsino dominated (LG10). Further, the associated sparticle spectrum is found to be widely different with the squarks and sleptons being as low as 200 GeV (or even less) in mass to being significantly heavy lying in the (2–3) TeV region. The models analyzed exhibit a wide array of sparticle mass hierarchies and signatures. It was shown that most of the models considered will be discoverable in the early runs at the LHC at $\sqrt{s} = 7$ TeV with 1 fb^{-1} of data while all the models will become visible with 5 fb^{-1} of integrated luminosity. The models considered are consistent with the stringent bounds on the annihilation of neutralinos into $\gamma\gamma$ and γZ from Fermi-LAT, and further many of the models considered are discoverable in the ongoing dark matter experiments, specifically CDMS-II, XENON100, and EDELWEISS-2. Further, it is found that some of the low mass gluino models (LG10, LG16, and LG17) can explain the positron excess observed in the satellite experiments such as PAMELA that probe antimatter in the Galaxy. It is shown that such models also lead to rich jet signatures at the LHC, thus representing a class of models which can be tested on multiple fronts.

ACKNOWLEDGMENTS

This research is supported in part by NSF Grant No. PHY-0653342 (Stony Brook), DOE Grant No. DE-FG02-95ER40899 (Michigan, MCTP), and NSF Grants No. PHY-0704067 and No. PHY-0757959 (Northeastern University), and in addition by the NSF through TeraGrid resources provided by National Center for Supercomputing Applications (NCSA), Texas Advanced Computing Center (TACC), Purdue University, and Louisiana Optical Network Initiative (LONI) under Grant No. TG-PHY100036. Discussions and/or communications with Ben Allanach, Darin Baumgartel, Gordon Kane, Ran Lu, Brent Nelson, Jing Shao, Robert Shrock, and Darien Wood are acknowledged.

[1] D. Feldman, Z. Liu, and P. Nath, Phys. Rev. Lett. **99**, 251802 (2007).
[2] D. Feldman, Z. Liu, and P. Nath, Phys. Lett. B **662**, 190 (2008).
[3] D. Feldman, Z. Liu, and P. Nath, J. High Energy Phys. 04 (2008) 054.
[4] J. A. Maxin, V. E. Mayes, and D. V. Nanopoulos, Phys. Rev. D **79**, 066010 (2009).
[5] C. F. Berger, J. S. Gainer, J. L. Hewett, and T. G. Rizzo, J. High Energy Phys. 02 (2009) 023; J. A. Conley, J. S. Gainer, J. L. Hewett, M. P. Le, and T. G. Rizzo, arXiv:1009.2539.
[6] S. AbdusSalam, B. Allanach, F. Quevedo, F. Feroz, and M. Hobson, Phys. Rev. D **81**, 095012 (2010).
[7] P. Konar, K. T. Matchev, M. Park, and G. K. Sarangi, Phys. Rev. Lett. **105**, 221801 (2010).
[8] A. Atre, Y. Bai, and E. Eichten, Proceedings of the Low Emittance Muon Collider Workshop—April 2008 (unpublished), http://www.muonsinc.com/lemc2008/presentations/lemc_apr08.pdf.
[9] P. Nath *et al.*, Nucl. Phys. B, Proc. Suppl. **200**, 185 (2010); W. Porod, arXiv:1010.4737.
[10] D. Feldman, Z. Liu, and P. Nath, Phys. Rev. D **81**, 095009 (2010).
[11] H. Baer, V. Barger, A. Lessa, and X. Tata, J. High Energy Phys. 06 (2010) 102.
[12] B. Altunkaynak, M. Holmes, P. Nath, B. D. Nelson, and G. Peim, Phys. Rev. D **82**, 115001 (2010).
[13] D. Feldman, G. Kane, R. Lu, and B. D. Nelson, Phys. Lett. B **687**, 363 (2010).
[14] G. F. Giudice, T. Han, K. Wang, and L. T. Wang, Phys. Rev. D **81**, 115011 (2010).
[15] D. S. M. Alves, E. Izaguirre, and J. G. Wacker, arXiv:1008.0407.
[16] H. K. Dreiner, M. Kramer, J. M. Lindert, and B. O'Leary, J. High Energy Phys. 04 (2010) 109; N. Bhattacharyya, A. Datta, and S. Poddar, Phys. Rev. D **82**, 035003 (2010); K. Desch, H. K. Dreiner, S. Fleischmann, S. Grab, and P. Wienemann, arXiv:1008.1580; B. Dutta, T. Kamon, A. Krislock, N. Kolev, and Y. Oh, Phys. Rev. D **82**, 115009 (2010); S. Abel, M. J. Dolan, J. Jaeckel, and V. V. Khoze, J. High Energy Phys. 12 (2010) 049; H. Baer, S. Kraml, A. Lessa, and S. Sekmen, J. High Energy Phys. 02 (2010) 055; B. C. Allanach, S. Grab, and H. E. Haber, arXiv:1010.4261.
[17] N. Chen, D. Feldman, Z. Liu, P. Nath, and G. Peim, Phys. Rev. D **83**, 023506 (2011).
[18] A. H. Chamseddine, R. Arnowitt, and P. Nath, Phys. Rev. Lett. **49**, 970 (1982); Nucl. Phys. **B227**, 121 (1983); L.

Hall, J. Lykken, and S. Weinberg, Phys. Rev. D **27**, 2359 (1983); for a review, see P. Nath, arXiv:hep-ph/0307123.

[19] A. Corsetti and P. Nath, Phys. Rev. D **64**, 125010 (2001); A. Birkedal-Hansen and B. D. Nelson, Phys. Rev. D **64**, 015008 (2001); U. Chattopadhyay and P. Nath, Phys. Rev. D **65**, 075009 (2002); **65**, 075009 (2002); G. L. Kane, J. D. Lykken, S. Mrenna, B. D. Nelson, L. T. Wang, and T. T. Wang, Phys. Rev. D **67**, 045008 (2003); **67**, 095006 (2003); D. G. Cerdeno and C. Munoz, J. High Energy Phys. 10 (2004) 015; S. F. King, J. P. Roberts, and D. P. Roy, J. High Energy Phys. 10 (2007) 106.

[20] H. Baer, A. Mustafayev, E. K. Park, and X. Tata, J. High Energy Phys. 05 (2008) 058; J. R. Ellis, K. A. Olive, and P. Sandick, J. High Energy Phys. 08 (2008) 013; B. Altunkaynak, M. Holmes, and B. D. Nelson, J. High Energy Phys. 10 (2008) 013; S. P. Martin, Phys. Rev. D **78**, 055019 (2008); S. Bhattacharya, A. Datta, and B. Mukhopadhyaya, Phys. Rev. D **78**, 115018 (2008); U. Chattopadhyay and D. Das, Phys. Rev. D **79**, 035007 (2009); S. Bhattacharya, U. Chattopadhyay, D. Choudhury, D. Das, and B. Mukhopadhyaya, Phys. Rev. D **81**, 075009 (2010).

[21] D. Feldman, B. Kors, and P. Nath, Phys. Rev. D **75**, 023503 (2007).

[22] D. Feldman, Z. Liu, P. Nath, and B. D. Nelson, Phys. Rev. D **80**, 075001 (2009); D. Feldman, Nucl. Phys. B, Proc. Suppl. **200**, 82 (2010).

[23] D. Feldman, Z. Liu, and P. Nath, Phys. Rev. D **79**, 063509 (2009); M. Ibe, H. Murayama, and T. T. Yanagida, Phys. Rev. D **79**, 095009 (2009); W. L. Guo and Y. L. Wu, Phys. Rev. D **79**, 055012 (2009).

[24] For recent work in the context of multistate dark matter, see D. Feldman, Z. Liu, P. Nath, and G. Peim, Phys. Rev. D **81**, 095017 (2010); S. S. AbdusSalam and F. Quevedo, arXiv:1009.4308.

[25] T. Moroi and L. Randall, Nucl. Phys. **B570**, 455 (2000); for recent work, see, e.g., B. S. Acharya, G. Kane, S. Watson, and P. Kumar, Phys. Rev. D **80**, 083529 (2009).

[26] For a recent review, see D. Feldman and G. Kane, in *Perspectives on Supersymmetry II* (World Scientific, Singapore, 2010).

[27] A. A. Abdo *et al.*, Phys. Rev. Lett. **104**, 091302 (2010).

[28] Z. Ahmed *et al.* (CDMS Collaboration), Phys. Rev. Lett. **102**, 011301 (2009); Science **327**, 1619 (2010).

[29] E. Aprile *et al.* (XENON100 Collaboration), Phys. Rev. Lett. **105**, 131302 (2010).

[30] Valentin Kozlov for the EDELWEISS Collaboration, arXiv:1010.5947.

[31] J. L. Feng and D. Sanford, arXiv:1009.3934.

[32] O. Adriani *et al.* (PAMELA Collaboration), Nature (London) **458**, 607 (2009); Phys. Rev. Lett. **102**, 051101 (2009).

[33] N. Jarosik *et al.* (WMAP Collaboration), arXiv:1001.4744; E. Komatsu *et al.* (WMAP Collaboration), Astrophys. J. Suppl. Ser. **180**, 330 (2009); D. N. Spergel *et al.* (WMAP Collaboration), Astrophys. J. Suppl. Ser. **170**, 377 (2007).

[34] K. L. Chan, U. Chattopadhyay, and P. Nath, Phys. Rev. D **58**, 096004 (1998); J. L. Feng, K. T. Matchev, and T. Moroi, Phys. Rev. Lett. **84**, 2322 (2000); U. Chattopadhyay, A. Corsetti, and P. Nath, Phys. Rev. D **68**, 035005 (2003); H. Baer, C. Balazs, A. Belyaev, T. Krupovnickas, and X. Tata, J. High Energy Phys. 06 (2003) 054.

[35] M. Misiak *et al.*, Phys. Rev. Lett. **98**, 022002 (2007).

[36] G. Degrassi, P. Gambino, and G. F. Giudice, J. High Energy Phys. 12 (2000) 009; F. Borzumati, C. Greub, T. Hurth, and D. Wyler, Phys. Rev. D **62**, 075005 (2000); M. E. Gomez, T. Ibrahim, P. Nath, and S. Skadhauge, Phys. Rev. D **74**, 015015 (2006).

[37] N. Chen, D. Feldman, Z. Liu, and P. Nath, Phys. Lett. B **685**, 174 (2010).

[38] T. Aaltonen *et al.* (CDF Collaboration), Phys. Rev. Lett. **100**, 101802 (2008).

[39] D. Feldman, Z. Liu, and P. Nath, Phys. Rev. D **81**, 117701 (2010); E. Kuflik, A. Pierce, and K. M. Zurek, Phys. Rev. D **81**, 111701 (2010); D. A. Vasquez, G. Belanger, C. Boehm, A. Pukhov, and J. Silk, arXiv:1009.4380; see also D. Das and U. Ellwanger, J. High Energy Phys. 09 (2010) 085; A. V. Belikov, J. F. Gunion, D. Hooper, and T. M. P. Tait, arXiv:1009.0549; arXiv:1009.2555; P. Draper, T. Liu, C. E. M. Wagner, Lian-Tao Wang, and H. Zhang, arXiv:1009.3963; J. F. Gunion, arXiv:1010.1789.

[40] R. Bernabei *et al.*, Eur. Phys. J. C **67**, 39 (2010).

[41] C. E. Aalseth *et al.* (CoGeNT Collaboration), arXiv:1002.4703 [Phys. Rev. Lett. (to be published)].

[42] T. C. Yuan, R. L. Arnowitt, A. H. Chamseddine, and P. Nath, Z. Phys. C **26**, 407 (1984); D. A. Kosower, L. M. Krauss, and N. Sakai, Phys. Lett. **133B**, 305 (1983); J. L. Lopez, D. V. Nanopoulos, and X. Wang, Phys. Rev. D **49**, 366 (1994); U. Chattopadhyay and P. Nath, Phys. Rev. Lett. **86**, 5854 (2001).

[43] G. W. Bennett *et al.* (Muon $g-2$ Collaboration), Phys. Rev. Lett. **92**, 161802 (2004).

[44] M. Davier, A. Hoecker, B. Malaescu, C. Z. Yuan, and Z. Zhang, Eur. Phys. J. C **66**, 1 (2010).

[45] Q. H. Cao, E. Ma, J. Wudka, and C. P. Yuan, arXiv:0711.3881.

[46] T. Hur, H. S. Lee, and S. Nasri, Phys. Rev. D **77**, 015008 (2008).

[47] C. Boehm, P. Fayet, and J. Silk, Phys. Rev. D **69**, 101302 (2004).

[48] S. P. Martin, Phys. Rev. D **79**, 095019 (2009).

[49] P. Nath, R. L. Arnowitt, and A. H. Chamseddine, in *Proceedings of the Workshop on Problems in Unication and Supergravity, La Jolla Institute, 1983* (World Scientific, Singapore, (1983); L. Alvarez-Gaume, J. Polchinski, and M. B. Wise, Nucl. Phys. **B221**, 495 (1983).

[50] D. Feldman, Z. Liu, and P. Nath, Phys. Rev. D **80**, 015007 (2009).

[51] I. Gogoladze, R. Khalid, S. Raza, and Q. Shafi, arXiv:1008.2765; I. Gogoladze, R. Khalid, and Q. Shafi, Phys. Rev. D **80**, 095016 (2009); **79**, 115004 (2009).

[52] L. Covi, M. Olechowski, S. Pokorski, K. Turzynski, and J. D. Wells, arXiv:1009.3801.

[53] R. L. Arnowitt and P. Nath, Phys. Rev. D **46**, 3981 (1992).

[54] H. Baer, V. Barger, G. Shaughnessy, H. Summy, and L. t. Wang, Phys. Rev. D **75**, 095010 (2007).

[55] D. Feldman, Z. Liu, and P. Nath, Phys. Rev. D **78**, 083523 (2008).

[56] P. Nath and R. L. Arnowitt, Phys. Rev. Lett. **70**, 3696 (1993); A. Djouadi, M. Drees, and J. L. Kneur, Phys. Lett. B **624**, 60 (2005).

[57] R. L. Arnowitt and P. Nath, Phys. Rev. Lett. **69**, 725 (1992).

[58] K. Griest and D. Seckel, Phys. Rev. D **43**, 3191 (1991).

[59] S. Profumo, Phys. Rev. D **72**, 103521 (2005); S. Profumo and C. Yaguna, Phys. Rev. D **69**, 115009 (2004).

[60] H. Baer, K. m. Cheung, and J. F. Gunion, Phys. Rev. D **59**, 075002 (1999); S. Raby and K. Tobe, Nucl. Phys. **B539**, 3 (1999).

[61] O. Adriani *et al.* (PAMELA Collaboration), Astropart. Phys. **34**, 1 (2010).

[62] O. Adriani *et al.* (PAMELA Collaboration), Phys. Rev. Lett. **105**, 121101 (2010).

[63] M. A. DuVernois *et al.*, Astrophys. J. **559**, 296 (2001); J. J. Beatty *et al.*, Phys. Rev. Lett. **93**, 241102 (2004); M. Aguilar *et al.* (AMS-01 Collaboration), Phys. Lett. B **646**, 145 (2007).

[64] B. Kors and P. Nath, Phys. Lett. B **586**, 366 (2004); J. High Energy Phys. 12 (2004) 005; 07 (2005) 069.

[65] K. R. Dienes, C. F. Kolda, and J. March-Russell, Nucl. Phys. **B492**, 104 (1997).

[66] D. Feldman, Z. Liu, and P. Nath, Phys. Rev. Lett. **97**, 021801 (2006); J. High Energy Phys. 11 (2006) 007; Phys. Rev. D **75**, 115001 (2007); K. Cheung and T. C. Yuan, J. High Energy Phys. 03 (2007) 120; J. Kumar and J. D. Wells, Phys. Rev. D **74**, 115017 (2006); W. F. Chang, J. N. Ng, and J. M. S. Wu, Phys. Rev. D **75**, 115016 (2007); S. Gopalakrishna, S. Jung, and J. D. Wells, Phys. Rev. D **78**, 055002 (2008); Y. Mambrini, J. Cosmol. Astropart. Phys. 09 (2010) 022; A. Hook, E. Izaguirre, and J. G. Wacker, arXiv:1006.0973; K. L. McDonald and D. E. Morrissey, arXiv:1010.5999.

[67] F. Fucito, A. Lionetto, A. Mammarella, and A. Racioppi, Eur. Phys. J. C **69**, 455 (2010); C. Coriano, M. Guzzi, G. Lazarides, and A. Mariano, Phys. Rev. D **82**, 065013 (2010); arXiv:1010.2010; K. Cheung, K. H. Tsao, and T. C. Yuan, arXiv:1003.4611; E. Dudas, Y. Mambrini, S. Pokorski, and A. Romagnoni, J. High Energy Phys. 08 (2009) 014; Y. Mambrini, J. Cosmol. Astropart. Phys. 12 (2009) 005.

[68] A. Arvanitaki, N. Craig, S. Dimopoulos, S. Dubovsky, and J. March-Russell, Phys. Rev. D **81**, 075018 (2010).

[69] L. J. Hall, K. Jedamzik, J. March-Russell, and S. M. West, J. High Energy Phys. 03 (2010) 080.

[70] S. Profumo and A. Provenza, J. Cosmol. Astropart. Phys. 12 (2006) 019.

[71] G. L. Kane, L. T. Wang, and J. D. Wells, Phys. Rev. D **65**, 057701 (2002); E. A. Baltz, J. Edsjo, K. Freese, and P. Gondolo, Phys. Rev. D **65**, 063511 (2002); D. Hooper and J. Silk, Phys. Rev. D **71**, 083503 (2005).

[72] G. Kane, R. Lu, and S. Watson, Phys. Lett. B **681**, 151 (2009); J. Hisano, M. Kawasaki, K. Kohri, and K. Nakayama, Phys. Rev. D **79**, 063514 (2009).

[73] A. W. Strong and I. V. Moskalenko, Astrophys. J. **509**, 212 (1998); E. A. Baltz and J. Edsjo, Phys. Rev. D **59**, 023511 (1998); L. Bergstrom, J. Edsjo, and P. Ullio, Astrophys. J. **526**, 215 (1999); P. Gondolo, J. Edsjo, P. Ullio, L. Bergstrom, M. Schelke, and E. A. Baltz, J. Cosmol. Astropart. Phys. 07 (2004) 008; J. Hisano, S. Matsumoto, O. Saito, and M. Senami, Phys. Rev. D **73**, 055004 (2006); M. Cirelli, R. Franceschini, and A. Strumia, Nucl. Phys. **B800**, 204 (2008); M. Cirelli, M. Kadastik, M. Raidal, and A. Strumia, Nucl. Phys. **B813**, 1 (2009).

[74] J. F. Navarro, C. S. Frenk, and S. D. M. White, Astrophys. J. **490**, 493 (1997); B. Moore, T. R. Quinn, F. Governato, J. Stadel, and G. Lake, Mon. Not. R. Astron. Soc. **310**, 1147 (1999); P. Salucci and A. Burkert, Astrophys. J. **537**, L9 (2000).

[75] Fermi LAT Collaboration, Phys. Rev. D **82**, 092004 (2010).

[76] J. Alwall *et al.*, J. High Energy Phys. 09 (2007) 028.

[77] T. Sjostrand, S. Mrenna, and P. Z. Skands, J. High Energy Phys. 05 (2006) 026.

[78] J. Conway *et al.*, PGS-4.

[79] G. Aad *et al.* (ATLAS Collaboration), arXiv:0901.0512.

[80] G. L. Bayatian *et al.* (CMS Collaboration), *Detector Performance and Software*, CMS technical design report, Vol. I (LHCC, Geneva, 2006).

[81] S. Jadach, Z. Was, R. Decker, and J. H. Kuhn, Comput. Phys. Commun. **76**, 361 (1993).

[82] A. Djouadi, J. L. Kneur, and G. Moultaka, Comput. Phys. Commun. **176**, 426 (2007).

[83] G. Belanger, F. Boudjema, A. Pukhov, and A. Semenov, Comput. Phys. Commun. **180**, 747 (2009).

[84] M. Muhlleitner, A. Djouadi, and Y. Mambrini, Comput. Phys. Commun. **168**, 46 (2005); A. Djouadi, M. M. Muhlleitner, and M. Spira, Acta Phys. Pol. B **38**, 635 (2007).

[85] B. C. Allanach, Comput. Phys. Commun. **143**, 305 (2002).

[86] P. Nath and R. L. Arnowitt, Mod. Phys. Lett. A **2**, 331 (1987); R. L. Arnowitt, R. M. Barnett, P. Nath, and F. Paige, Int. J. Mod. Phys. A **2**, 1113 (1987); H. Baer and X. Tata, Phys. Rev. D **47**, 2739 (1993); for a recent analysis, see Z. Sullivan and E. L. Berger, Phys. Rev. D **78**, 034030 (2008).